

Anisotropic space-time goal-oriented error control and mesh adaptivity for convection-diffusion-reaction equations

M. Bause¹, M. P. Bruchhäuser¹, B. Endtmayer^{2,3}, N. Margenberg¹, I. Touloupoulos⁴, and T. Wick^{2,3}

¹Helmut Schmidt University, University of the German Federal Armed Forces Hamburg, Faculty of Mechanical and Civil Engineering, Chair of Numerical Mathematics, Holstenhofweg 85, 22043 Hamburg, Germany

²Leibniz Universität Hannover, Institut für Angewandte Mathematik, Welfengarten 1, 30167 Hannover, Germany

³Cluster of Excellence PhoenixD (Photonics, Optics, and Engineering – Innovation Across Disciplines), Leibniz Universität Hannover, Germany

⁴University of Western Macedonia, Department of Informatics, Fourka Area, 52100 Kastoria, Greece

April 22, 2025

Abstract

We present an anisotropic goal-oriented error estimator based on the Dual Weighted Residual (DWR) method for time-dependent convection-diffusion-reaction (CDR) equations. Using anisotropic interpolation operators the estimator is elementwise separated with respect to the single directions in space and time leading to adaptive, anisotropic mesh refinement in a natural way. To prevent spurious oscillations the streamline upwind Petrov-Galerkin (SUPG) method is applied to stabilize the underlying system in the case of high Péclet numbers. Efficiency and robustness of the underlying algorithm are demonstrated for different goal functionals. The directional error indicators quantify anisotropy of the solution with respect to the goal, and produce meshes that efficiently capture sharp layers. Numerical examples show the superiority of the proposed approach over isotropic adaptive and global mesh refinement using established benchmarks for convection-dominated transport.

Keywords: Space-time finite elements, goal-oriented error control, dual weighted residual method, Anisotropic adaptation, SUPG stabilization

1 Introduction

Adaptive finite element methods (AFEM) are essential for solving partial differential equations with localized phenomena such as layers, shocks, or singularities. For applications involving such phenom-

ena, convection-diffusion-reaction (CDR) equations have been established as a prototypical model for more sophisticated systems of interest in practice, for instance, the Navier-Stokes equations. Their numerical solution remains an active topic of research. Following John et al. [36], we regard a numerical solution *adequate* if it (O1) captures *sharp layers*, (O2) does not exhibit *spurious oscillations* and (O3) is *feasible* and *efficient* to compute. In the past, a lot of effort has been spent on addressing the objectives (O1) and (O2). Typically, these issues are addressed by means of stabilization. For many years, the streamline upwind Petrov–Galerkin (SUPG) method [35, 14] and other residual-based stabilizations have been the most widely used techniques. Another approach that has gained traction is the class of algebraically stabilized schemes, which relies on the algebraic system from the Galerkin finite element discretization and introduce limiters for controlling the slopes of the concrete solution. For a review of flux corrected transport we refer to [42, 43] and references therein. We refer to [51, 6, 55, 36] for a general review of stabilization techniques. For a numerical comparison related to time-dependent CDR equations we refer to [38, 22]. In this work we address (O1) and (O2) through SUPG stabilization. We aim to address (O3) by means of *economic* discretizations which lead to efficient numerical solutions. To the best of our knowledge, only few key contributions on this topic have been made in recent years and there remains potential for improvement towards (O3). In many applications only certain quantities are of interest. Adaptation with respect to these quantities improves efficiency significantly. Adjoint-based error estimation provides the tools for this goal-oriented approach. Specifically, we use the Dual Weighted Residual (DWR) method [10]. DWR has been applied successfully to parabolic convection-dominated problems in previous work by some of the authors [16, 8, 15]. Goal oriented error estimation with isotropic mesh adaptivity for space time problems using the DWR method can be found in [53, 11, 26, 52, 29, 54, 25]. A framework for mesh adaptation with a high order DG discretization has been presented [58]. In [19] and references therein, these concepts have been generalized to anisotropic space-time adaptation. Furthermore, adaptively refined meshes are essential for numerical stability: On globally refined meshes even stabilization schemes fail to reduce oscillations near steep gradients (cf. [38]).

The computational efficiency of AFEM can be improved through *anisotropic* refinement along dominant error directions. This approach has been successfully applied to many fields, e.g. [21, 59, 19, 48, 58, 47, 44, 30, 32, 31, 45, 56]. Anisotropic mesh refinement applied to CDR problems can be found in [39, 58, 33, 32, 5, 41]. For a general overview of anisotropic finite elements we refer to the monograph of Apel [4].

To address (O3) and achieve *economic* discretizations, we propose an *anisotropic space-time goal-oriented mesh adaptation* framework. Motivated by ideas of Richter [47, 48], we combine goal-oriented error estimation with anisotropic refinement. Our proposed method provides directional error indicators in space and time with respect to a user-defined goal. Thereby, the directional separation of elementwise indicators naturally leads to anisotropic mesh refinement.

Our approach automatically identifies dominant error directions. This represents one of the key challenges to other approaches using anisotropic mesh refinement. To this end, a frequently used approach involves the analysis of the Hessian matrix [44, 30, 32]. Its eigenvectors indicate the major

refinement directions, while the eigenvalues quantify the strength of the anisotropy. This method has been successfully applied in various settings. However, Hessian-based approaches face two key limitations. First, it is unclear whether refinement should be based on the Hessian of the primal solution u or the adjoint solution z , as anisotropic influences may be caused by both variables, as explained in [47]. Second, the Hessian is most effective when using linear finite elements. For higher-order finite elements, the Hessian does not provide reliable error information since second-order curvature is already captured by the method [49, Sec. 8.4]. By directly estimating directional errors within the DWR framework these limitations are circumvented and a refinement strategy that accounts for both primal and adjoint residuals is achieved.

The contribution of this work is twofold: (1) we develop a framework for anisotropic space-time mesh adaptation which captures directional solution features, and (2) we integrate goal-oriented error estimation to refine the mesh where it most impacts the goal, leading to computationally efficient and economic space-time discretizations. The implementation builds on the approaches presented in [40, 8, 16]. Notably, aside from a few extra interpolation steps, estimating directional errors incurs no additional computational cost compared to the DWR method used in [40, 8, 16].

The remainder of this work is organized as follows: In Sec. 2, we introduce the CDR equation and its variational formulation. Sec. 3 outlines the space-time discretization and reviews the classical isotropic error representation as a starting point for further development. The main contribution is presented in Sec. 4, where we detail an anisotropic error estimation technique. In Sec. 5, we describe the algorithm for goal-oriented anisotropic mesh refinement. Finally, Sec. 6 illustrates and validates our approach by numerical examples, including comparisons with isotropic refinement.

2 Model Problem and Variational Formulation

As a model problem, we study the following time-dependent CDR equation:

$$\begin{aligned} \partial_t u - \nabla \cdot (\varepsilon \nabla u) + \mathbf{b} \cdot \nabla u + \alpha u &= f \quad \text{in } \mathcal{Q} = \Omega \times I, \\ u &= u_D \quad \text{on } \Sigma_D = \Gamma_D \times I, \\ \varepsilon \nabla u \cdot \mathbf{n} &= u_N \quad \text{on } \Sigma_N = \Gamma_N \times I, \\ u(0) &= u_0 \quad \text{on } \Sigma_0 = \Omega \times \{0\}, \end{aligned} \tag{1}$$

in the space-time domain \mathcal{Q} , where $\Omega \subset \mathbb{R}^d$, with $d = 2$ or $d = 3$, is a polygonal or polyhedral bounded domain with Lipschitz boundary $\partial\Omega$ and $I = (0, T)$, $0 < T < \infty$, is a finite time interval. Here, $\partial\Omega = \Gamma_D \cup \Gamma_N$, $\Gamma_D \neq \emptyset$ denotes the partition of the boundary with outer unit normal vector \mathbf{n} , where Γ_D denotes the Dirichlet part and Γ_N the Neumann part, respectively. Furthermore, let $V := \{v \in H^1(\Omega) | v|_{\Gamma_D} = 0\}$ and V' denotes the adjoint space of V . To ensure the well-posedness of Eq. (1) we assume that $0 < \varepsilon \leq 1$ is a constant diffusion coefficient, $\mathbf{b} \in L^\infty(I; W^{1,\infty}(\Omega)^d)$ is the flow field or convection field, $\alpha \in L^\infty(I; L^\infty(\Omega))$ is a non-negative ($\alpha \geq 0$) reaction coefficient, $u_0 \in L^2(\Omega)$ is a given initial condition, $f \in L^2(I; V')$ is a given source of the unknown scalar quantity u , $u_D \in L^2(I; H^{\frac{1}{2}}(\Gamma_D))$ is a given function specifying the Dirichlet boundary condition, and $u_N \in L^2(I; H^{-\frac{1}{2}}(\Gamma_N))$ is a given function specifying the Neumann boundary condition. Furthermore, it

will be assumed that either $\nabla \cdot \mathbf{b}(\mathbf{x}, t) = 0$ and $\alpha(\mathbf{x}, t) \geq 0$, or there exists a positive constant c_0 such that $\alpha(\mathbf{x}, t) - \frac{1}{2} \operatorname{div} \mathbf{b}(\mathbf{x}, t) \geq c_0 > 0 \quad \forall (\mathbf{x}, t) \in \bar{\Omega} \times \bar{I}$, which are standard assumptions for convection-dominated equations of type (1), cf., e.g., [2, 51].

Henceforth, for the sake of simplicity, we deal with homogeneous Dirichlet boundary values $u_D = 0$ on $\Gamma_D = \partial\Omega$ only. This implies that here $V := H_0^1(\Omega)$. In the numerical examples in Sec. 6, we also consider more general boundary conditions, which are incorporated as described in [7, Ch. 3.3].

It is well known that problem (1) along with the above conditions admits a unique weak solution $u \in \mathcal{V} := \{v \in L^2(I; V) \mid \partial_t v \in L^2(I; V')\}$, that satisfies the following variational formulation; cf., e.g. [51, 36].

Problem 2.1. *Find $u \in \mathcal{V}$ such that*

$$A(u)(\varphi) = F(\varphi) \quad \forall \varphi \in \mathcal{V}, \quad (2)$$

where the bilinear form $A : \mathcal{V} \times \mathcal{V} \rightarrow \mathbb{R}$ and the linear form $F : \mathcal{V} \rightarrow \mathbb{R}$ are defined by

$$A(u)(\varphi) := \int_I \{(\partial_t u, \varphi) + a(u)(\varphi)\} dt + (u(0), \varphi(0)), \quad (3)$$

$$F(\varphi) := \int_I (f, \varphi) dt + (u_0, \varphi(0)), \quad (4)$$

with the inner bilinear form $a : V \times V \rightarrow \mathbb{R}$, given by

$$a(u)(\varphi) := (\varepsilon \nabla u, \nabla \varphi) + (\mathbf{b} \cdot \nabla u, \varphi) + (\alpha u, \varphi). \quad (5)$$

We note that the initial condition is incorporated into the variational problem. The weak formulation, given by Eq. (2), is now the starting point for the variational discretization in space and time using Galerkin finite element methods.

Later the aim of this work is the accurate approximation of a specific quantity of interest $J(u)$, defined by a functional $J \in \mathcal{C}^3(\mathcal{V}, \mathbb{R})$, where $u \in \mathcal{V}$ solves the model problem (2).

3 Space-Time Discretization and Isotropic Error Representation

In this section, we present the space-time finite element discretization of our model problem including SUPG stabilization and, for completeness, review a goal-oriented error representation based on the DWR method for the isotropic case.

3.1 Discretization in Time

For the discretization in time we use a discontinuous Galerkin method $dG(r)$ with an arbitrary polynomial degree $r \geq 0$. Let \mathcal{T}_τ be a partition of the closure of the time domain $\bar{I} = [0, T]$ into left-open subintervals $I_n := (t_{n-1}, t_n]$, $n = 1, \dots, N$, with $0 =: t_0 < t_1 < \dots < t_N =: T$ and time step sizes $\tau_n = t_n - t_{n-1}$ and the global time discretization parameter $\tau = \max_n \tau_n$. Since the set of time intervals I_n is finite, it is natural to partition the global space-time cylinder $\mathcal{Q} = \Omega \times I$ into space-time slabs defined as $\mathcal{Q}_n = \Omega \times I_n$. On the subintervals I_n , we define the time-discrete function space \mathcal{V}_τ^r

$$\mathcal{V}_\tau^r := \left\{ u_\tau \in L^2(I; V) \mid u_\tau|_{I_n} \in \mathcal{P}_r(I_n; V), u_\tau(0) \in L^2(\Omega), n = 1, \dots, N \right\}, \quad (6)$$

where $\mathcal{P}_r(\bar{I}_n; V)$ denotes the space of all polynomials in time up to degree $r \geq 0$ on I_n with values in V . For some discontinuous in time function $u_\tau \in \mathcal{V}_\tau^r$ we define the limits $u_{\tau,n}^\pm$ from above and below of u_τ at t_n as well as their jump at t_n by

$$u_{\tau,n}^\pm := \lim_{t \rightarrow t_n \pm 0} u_\tau(t), \quad [u_\tau]_n := u_{\tau,n}^+ - u_{\tau,n}^-.$$

Then, the semi-discrete in time scheme of Eq. (2) reads as follows: *Find $u_\tau \in \mathcal{V}_\tau^r$ such that*

$$A_\tau(u_\tau)(\varphi_\tau) = F_\tau(\varphi_\tau) \quad \forall \varphi_\tau \in \mathcal{V}_\tau^r, \quad (7)$$

where the bilinear form $A_\tau(\cdot)(\cdot)$ and the linear form $F_\tau(\cdot)$ are defined by

$$A_\tau(u_\tau)(\varphi_\tau) := \sum_{n=1}^N \int_{I_n} \{(\partial_t u_\tau, \varphi_\tau) + a(u_\tau)(\varphi_\tau)\} dt + \sum_{n=2}^N ([u_\tau]_{n-1}, \varphi_{\tau,n-1}^+) + (u_{\tau,0}^+, \varphi_{\tau,0}^+), \quad (8)$$

$$F_\tau(\varphi_\tau) := \int_I (f, \varphi) dt + (u_0, \varphi_{\tau,0}^+), \quad (9)$$

with the inner bilinear form $a(\cdot)(\cdot)$ being defined by Eq. (5).

3.2 Discretization in Space and Stabilization

Next, we describe the Galerkin finite element approximation in space for the semi-discrete time scheme (7). We use Lagrange-type finite element spaces of continuous, piecewise polynomial functions. The spatial discretization is based on a decomposition \mathcal{T}_h of the domain Ω into disjoint elements K , such that $\bar{\Omega} = \cup_{K \in \mathcal{T}_h} \bar{K}$. For $d = 2, 3$, we use quadrilateral and hexahedral elements, respectively. Each element $K \in \mathcal{T}_h$ is mapped from the reference element $\hat{K} = (0, 1)^d$ via an iso-parametric transformation $\mathbf{T}_K : \hat{K} \rightarrow K$ satisfying $\det(\mathbf{T}_K)(\hat{x}) > 0$ for all $\hat{x} \in (0, 1)^d$. Following [47], we decompose

$$\mathbf{T}_K := \mathbf{R}_K \circ \mathbf{S}_{c,K} \circ \mathbf{S}_{h,K} \circ \mathbf{P}_K, \quad (10)$$

where \mathbf{R}_K is a rotation and translation, $\mathbf{S}_{c,K}$ an anisotropic scaling, $\mathbf{S}_{h,K}$ a shearing, and \mathbf{P}_K is a nonlinear component. To account for anisotropic elements, we relax the standard shape-regularity assumptions and require only uniform boundedness of $\mathbf{S}_{h,K}$ and \mathbf{P}_K for all $K \in \mathcal{T}_h$. The element diameter is denoted by h_K , with the global discretization parameter defined as $h := \max_{K \in \mathcal{T}_h} h_K$.

Our mesh adaptation procedure employs local refinement with hanging nodes. Global conformity of the finite element approach is preserved by eliminating degrees of freedom at hanging nodes via interpolation between neighboring regular nodes; see [7, Ch. 4.2] and [20].

Definition 3.1. *On a subsect $\mathcal{Z}_h \subseteq \mathcal{T}_h$, we define the discrete finite element space*

$$V_h^p(\mathcal{Z}_h) := \{v \in C(\bar{\Omega}) \mid v|_K \in Q_p(K), \forall K \in \mathcal{Z}_h\} \cap V,$$

where, $Q_p(K)$ is the mapped finite element from

$$\hat{Q}_p(\hat{K}) := \bigotimes_{i=1}^d \mathcal{P}_p([0, 1]),$$

by (10), where $\mathcal{P}_p([0, 1])$ is the space of univariate polynomials of degree p . On \mathcal{T}_h we put

$$V_h^p = V_h^p(\mathcal{T}_h).$$

Let the fully discrete function space be given by

$$\mathcal{V}_{\tau h}^{r,p} := \left\{ u_{\tau h} \in X_{\tau}^r \mid u_{\tau h}|_{I_n} \in \mathcal{P}_r(I_n; V_h^p), u_{\tau h}(0) \in V_h^p, n = 1, \dots, N \right\} \subseteq L^2(I; V). \quad (11)$$

We note that the spatial finite element space V_h^p is allowed to be different on all subintervals I_n which is natural in the context of a discontinuous Galerkin approximation of the time variable and allows dynamic mesh changes in time. Due to the conformity of V_h^p we get $\mathcal{V}_{\tau h}^{r,p} \subseteq \mathcal{V}_{\tau}^r$. Now, the fully discrete discontinuous in time scheme reads as follows: *Find $u_{\tau h} \in \mathcal{V}_{\tau h}^{r,p}$ such that*

$$A_{\tau}(u_{\tau h})(\varphi_{\tau h}) = F_{\tau}(\varphi_{\tau h}) \quad \forall \varphi_{\tau h} \in \mathcal{V}_{\tau h}^{r,p}, \quad (12)$$

with $A_{\tau}(\cdot)(\cdot)$, $a(\cdot)(\cdot)$ and $F_{\tau}(\cdot)$ being defined in (8), (5) and (9), respectively.

In this work, we focus on convection-dominated problems with small diffusion parameter $\varepsilon > 0$. Then, the finite element approximation needs to be stabilized in order to reduce spurious and non-physical oscillations of the discrete solution arising close to layers. Here, we apply the streamline upwind Petrov-Galerkin (SUPG) method [35, 14]. Existing convergence analyses in the natural norm of the underlying scheme including local and global error bounds can be found, for instance, in [51, Ch. III.4.3]. The stabilized variant of the fully discrete discontinuous in time scheme then reads as follows: *Find $u_{\tau h} \in \mathcal{V}_{\tau h}^{r,p}$ such that*

$$A_S(u_{\tau h})(\varphi_{\tau h}) = F_{\tau}(\varphi_{\tau h}) \quad \forall \varphi_{\tau h} \in \mathcal{V}_{\tau h}^{r,p}, \quad (13)$$

where the linear form $F_{\tau}(\cdot)$ is defined by Eq. (9) and the stabilized bilinear form $A_S(\cdot)(\cdot)$ is given by

$$A_S(u_{\tau h})(\varphi_{\tau h}) := A_{\tau}(u_{\tau h})(\varphi_{\tau h}) + S(u_{\tau h})(\varphi_{\tau h}). \quad (14)$$

Here, the SUPG stabilization bilinear form $S(\cdot)(\cdot)$ is defined by

$$\begin{aligned} S(u_{\tau h})(\varphi_{\tau h}) := & \sum_{n=1}^N \int_{I_n} \sum_{K \in \mathcal{T}_{h,n}} \delta_K (r(u_{\tau h}), \mathbf{b} \cdot \nabla \varphi_{\tau h})_K dt \\ & + \sum_{n=2}^N \sum_{K \in \mathcal{T}_{h,n}} \delta_K ([u_{\tau h}]_{n-1}, \mathbf{b} \cdot \nabla \varphi_{\tau h, n-1}^+)_K \\ & + \sum_{K \in \mathcal{T}_{h,1}} \delta_K (u_{\tau h,0}^+ - u_0, \mathbf{b} \cdot \nabla \varphi_{\tau h,0}^+)_K, \end{aligned} \quad (15)$$

where the residual term $r(\cdot)$ is defined by

$$r(u_{\tau h}) := \partial_t u_{\tau h} - \nabla \cdot (\varepsilon \nabla u_{\tau h}) + \mathbf{b} \cdot \nabla u_{\tau h} + \alpha u_{\tau h} - f. \quad (16)$$

Remark 3.2. The proper choice of the stabilization parameter δ_K is an important issue in the application of the SUPG approach; cf., e.g., [37, 38, 36] and the discussion therein. For time-dependent CDR problems an optimal error estimate for $\delta_K = O(h)$ is derived in [37]. In this work, we chose $\delta_K = \delta_0 h_K$, where $\delta_0 = 0.1$ and $h_K = \sqrt[4]{|K|}$ is the cell diameter.

3.3 Isotropic Goal Oriented Error Estimation

As the fundamental ideas translate to anisotropic error representation, we present an isotropic a posteriori error representation for the stabilized problem (13) based on the Dual Weighted Residual (DWR) method [10, 7, 9]. This representation is given in terms of a user-chosen goal functional

$$J(u) = \int_0^T J_1(u(t))dt + J_2(u(T)),$$

where J_1 and J_2 are three times differentiable functionals and each of them may be zero; cf. [53, 11]. Since we focus on anisotropic error estimation, we restrict this section to the main result and refer to [15, Ch. 4] for a detailed derivation in the context of CDR equations.

For the error representations in Theorem. 3.3, we introduce the following Lagrangian functionals $\mathcal{L} : \mathcal{V} \times \mathcal{V} \rightarrow \mathbb{R}$, $\mathcal{L}_\tau : \mathcal{V}_\tau^r \times \mathcal{V}_\tau^r \rightarrow \mathbb{R}$, and $\mathcal{L}_{\tau h} : \mathcal{V}_{\tau h}^{r,p} \times \mathcal{V}_{\tau h}^{r,p} \rightarrow \mathbb{R}$ by

$$\mathcal{L}(u, z) := J(u) + F(z) - A(u)(z), \quad (17a)$$

$$\mathcal{L}_\tau(u_\tau, z_\tau) := J(u_\tau) + F_\tau(z_\tau) - A_\tau(u_\tau)(z_\tau), \quad (17b)$$

$$\mathcal{L}_{\tau h}(u_{\tau h}, z_{\tau h}) := J(u_{\tau h}) + F_\tau(z_{\tau h}) - A_S(u_{\tau h})(z_{\tau h}) = \mathcal{L}_\tau(u_{\tau h}, z_{\tau h}) - S(u_{\tau h})(z_{\tau h}). \quad (17c)$$

In (17), the Lagrange multipliers z , z_τ , and $z_{\tau h}$ are called adjoint variables in contrast to the primal variables u , u_τ , and $u_{\tau h}$; cf. [11, 10]. The directional derivatives of the Lagrangian functionals (Gâteaux derivatives) with respect to their second argument yields the primal problems (2), (7), (13), while the directional derivative with respect to their first argument yields the adjoint problems given by

$$A'(u)(\varphi, z) = J'(u)(\varphi) \quad \forall \varphi \in \mathcal{V}, \quad (18a)$$

$$A'_\tau(u_\tau)(\varphi_\tau, z_\tau) = J'(u_\tau)(\varphi_\tau) \quad \forall \varphi_\tau \in \mathcal{V}_\tau^r, \quad (18b)$$

$$A'_S(u_{\tau h})(\varphi_{\tau h}, z_{\tau h}) = J'(u_{\tau h})(\varphi_{\tau h}) \quad \forall \varphi_{\tau h} \in \mathcal{V}_{\tau h}^{r,p}, \quad (18c)$$

where the definitions of $A'(\cdot)(\cdot, \cdot)$, $A'_\tau(\cdot)(\cdot, \cdot)$, $A'_S(\cdot)(\cdot, \cdot)$ are given in the appendix.

Theorem 3.3. *Let $\{u, z\} \in \mathcal{V} \times \mathcal{V}$, $\{u_\tau, z_\tau\} \in \mathcal{V}_\tau^r \times \mathcal{V}_\tau^r$, and $\{u_{\tau h}, z_{\tau h}\} \in \mathcal{V}_{\tau h}^{r,p} \times \mathcal{V}_{\tau h}^{r,p}$ denote the stationary points of \mathcal{L} , \mathcal{L}_τ , and $\mathcal{L}_{\tau h}$ on the different levels of discretization, i.e.,*

$$\mathcal{L}'(u, z)(\delta u, \delta z) = \mathcal{L}'_\tau(u, z)(\delta u, \delta z) = 0 \quad \forall \{\delta u, \delta z\} \in \mathcal{V} \times \mathcal{V},$$

$$\mathcal{L}'_\tau(u_\tau, z_\tau)(\delta u_\tau, \delta z_\tau) = 0 \quad \forall \{\delta u_\tau, \delta z_\tau\} \in \mathcal{V}_\tau^r \times \mathcal{V}_\tau^r,$$

$$\mathcal{L}'_{\tau h}(u_{\tau h}, z_{\tau h})(\delta u_{\tau h}, \delta z_{\tau h}) = 0 \quad \forall \{\delta u_{\tau h}, \delta z_{\tau h}\} \in \mathcal{V}_{\tau h}^{r,p} \times \mathcal{V}_{\tau h}^{r,p}.$$

Then, for the discretization errors in space and time we get the representation formulas

$$J(u) - J(u_\tau) = \frac{1}{2}\rho_\tau(u_\tau)(z - \tilde{z}_\tau) + \frac{1}{2}\rho_\tau^*(u_\tau, z_\tau)(u - \tilde{u}_\tau) + \mathcal{R}_\tau, \quad (19a)$$

$$\begin{aligned} J(u_\tau) - J(u_{\tau h}) &= \frac{1}{2}\rho_\tau(u_{\tau h})(z_\tau - \tilde{z}_{\tau h}) + \frac{1}{2}\rho_\tau^*(u_{\tau h}, z_{\tau h})(u_\tau - \tilde{u}_{\tau h}) \\ &\quad + \frac{1}{2}S(u_{\tau h})(\tilde{z}_{\tau h} + z_{\tau h}) + \frac{1}{2}S'(u_{\tau h})(\tilde{u}_{\tau h} - u_{\tau h}, z_{\tau h}) + \mathcal{R}_h, \end{aligned} \quad (19b)$$

where ρ_τ and ρ_τ^* are the primal and adjoint residuals based on the semi-discrete in time schemes, respectively, given by

$$\rho_\tau(u)(\varphi) := \mathcal{L}'_{\tau, z}(u, z)(\varphi) = F_\tau(\varphi) - A_\tau(u)(\varphi), \quad (20a)$$

$$\rho_\tau^*(u, z)(\varphi) := \mathcal{L}'_{\tau, u}(u, z)(\varphi) = J'(u)(\varphi) - A'_\tau(u)(\varphi, z). \quad (20b)$$

Here, $\{\tilde{u}_\tau, \tilde{z}_\tau\} \in \mathcal{V}_\tau^r \times \mathcal{V}_\tau^r$, and $\{\tilde{u}_{\tau h}, \tilde{z}_{\tau h}\} \in \mathcal{V}_{\tau h}^{r,p} \times \mathcal{V}_{\tau h}^{r,p}$ can be chosen arbitrarily and $\mathcal{R}_\tau, \mathcal{R}_h$ are higher-order remainder terms with respect to the errors $u - u_\tau, z - z_\tau$ and $u_\tau - u_{\tau h}, z_\tau - z_{\tau h}$, respectively.

3.4 Isotropic Patch-Wise Higher Order Interpolation

In this section we introduce the isotropic patch-wise higher order interpolation. This interpolation technique is widely used in goal-oriented error estimation (cf., e.g., [10, 7, 46, 50, 28]). We assume that \mathcal{T}_h has been once refined, i.e. $\mathcal{T}_h = R(\mathcal{T}_{2h})$, where R denotes the uniform refinement of a mesh.

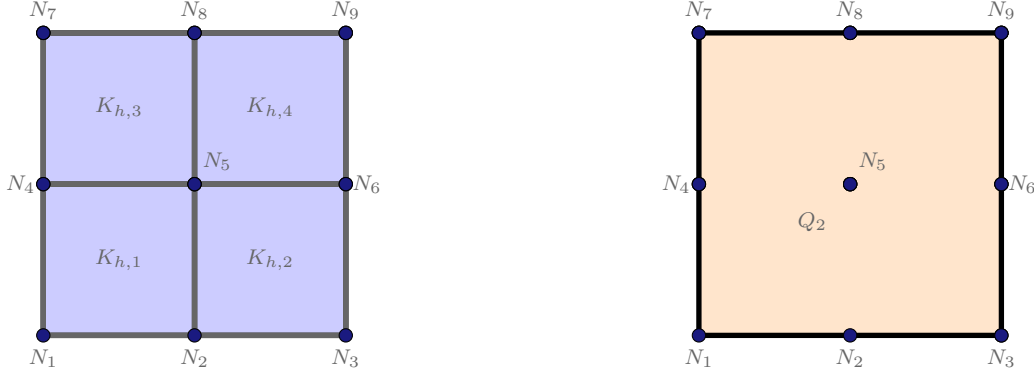


Figure 1: DoFs of Q_1 finite elements on the patch K_{2h}^P (left) and a the DoFs of a Q_2 finite element on the element K_{2h} (right).

To an element $K_{2h} \in \mathcal{T}_{2h}$, we uniquely associate the patch

$$K_{2h}^P := \{K \in \mathcal{T}_h : |K \cap K_{2h}| \neq 0\}, \quad (21)$$

and define the unique partitioning of \mathcal{T}_h into patches

$$\mathcal{T}_{2h}^P := \bigcup_{K_{2h} \in \mathcal{T}_{2h}} K_{2h}^P. \quad (22)$$

We note that, the degrees of freedom (DoFs) of $V_h^p(K_{2h}^P)$ coincide with the DoFs in $V_h^{2p}(K_{2h})$. We therefore enumerate the DoFs on $V_h^p(K_{2h}^P)$ and $V_h^{2p}(K_{2h})$ identically, from 1 to $N_{\text{DoF}}^P := \dim V_h^p(K_{2h}^P)$. For Q_1 and Q_2 finite elements this is visualized in Figure 1.

On the patches, we define the isotropic patch-wise higher order interpolation $I_{2h}^{(2p)}$ as in [7].

Definition 3.4. We define the bijective mapping $I_{2h}^{(2p, K_{2h})} : V_h^p(K_{2h}^P) \rightarrow V_h^{2p}(K_{2h})$ by

$$\left(I_{2h}^{(2p, K_{2h})} v_h \right) (N_j) = v_h(N_j) \quad \text{for } j = 1, \dots, N_{\text{DoF}}^P,$$

for all DoFs $N_j \in K_{2h}^P$ and $v_h \in V_h^p(K_{2h}^P)$. The global mapping $I_{2h}^{(2p)} : V_h^p(\mathcal{T}_h) \rightarrow V_h^{2p}(\mathcal{T}_{2h})$ is given by

$$I_{2h}^{(2p)} v_h(x) := \left(I_{2h}^{(2p, K_{2h})} v_h \right) (x) \quad \text{for } x \in K \subset K_{2h}^P, K_{2h}^P \in \mathcal{T}_{2h}^P. \quad (23)$$

For later computations, we also need the restriction operator on the reference element \hat{K} .

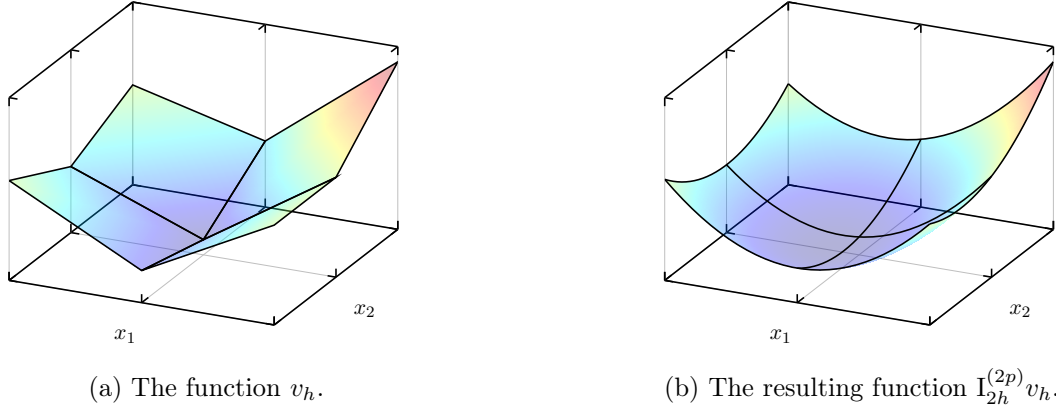


Figure 2: The action of $I_{2h}^{(2p)}$ of a Q_1 finite element function v_h on the patch K_{2h}^P .

Definition 3.5. Let $\hat{v}^{2p} \in \hat{Q}_{2p}(\hat{K})$. Then, the restriction $\hat{R}^{2p,p} : \hat{Q}_{2p}(\hat{K}) \rightarrow \hat{Q}_p(\hat{K})$ is defined as the unique function defined by the condition

$$\left(\hat{R}^{2p,p} \hat{v}^{2p} \right) (\hat{N}_j) = \hat{v}^{2p}(\hat{N}_j) \quad \text{for } j = 1, \dots, (p+1)^d, \quad (24)$$

where \hat{N}_j is a DoF on $\hat{Q}_p(\hat{K})$. We call $\hat{R}^{2p,p}$ the isotropic restriction operator on \hat{K} .

Definition 3.6. For $v_h \in \mathcal{V}_h^{2p}$, we define the restriction operator $R_h^p : \mathcal{V}_h^{2p} \rightarrow \mathcal{V}_h^p$ using the isoparametric mapping (10) and (24), as

$$(R_h^p v_h)(x) := \left(\hat{R}^{2p,p} \hat{v}_h \right) (\mathbf{T}_K^{-1}(x)), \quad x \in K, \quad (25)$$

with $\hat{v}_h = \mathbf{T}_K^{-1} \circ v_h$.

3.5 Local Error Indicators in Space and Time

For the practical use of the error representations (19) obtained in Theorem 3.3, we need to replace unknown quantities by computable ones. This requires multiple steps: First, we neglect the remainder terms \mathcal{R}_τ and \mathcal{R}_h in (19) as they are of higher order. Second, the unknown solutions in (19) are replaced by means of the approximated fully discrete solutions $u_{\tau h} \in \mathcal{V}_{\tau h}^{r,p}$ and $z_{\tau h} \in \mathcal{V}_{\tau h}^{r,q}$, with $q = 2p$, respectively. Third, the temporal and spatial weights have to be approximated in a suitable way, see [10, 7] for a short review of possible techniques. Here, we choose the following approximations for the temporal and spatial weights based on our previous numerical comparisons in [18, 17]:

Temporal Weights. Approximate the temporal weights $u - \tilde{u}_\tau$ and $z - \tilde{z}_\tau$, respectively, by means of a higher-order reconstruction using Gauss quadrature points given by

$$u - \tilde{u}_\tau \approx E_\tau^{(r+1)} u_{\tau h} - u_{\tau h}, \quad z - \tilde{z}_\tau \approx E_\tau^{(r+1)} z_{\tau h} - z_{\tau h},$$

using a reconstruction in time operator $E_\tau^{(r+1)}$ that lifts the solution to a piecewise polynomial of degree $(r+1)$ in time, cf. [17, 15] for further details.

Spatial Weights. Using the patch-wise higher-order interpolation operator (23) the restriction operator (25), we approximate the spatial weights $u_\tau - \tilde{u}_{\tau h}$, $z_\tau - \tilde{z}_{\tau h}$, and $\tilde{z}_{\tau h}$ via patch-wise higher-order interpolation and higher-order finite element approach as

$$u_\tau - \tilde{u}_{\tau h} \approx \mathbf{I}_{2h}^{(2p)} u_{\tau h} - u_{\tau h}, \quad z_\tau - \tilde{z}_{\tau h} \approx z_{\tau h} - \mathbf{R}_h^p z_{\tau h}, \quad \tilde{z}_{\tau h} \approx \mathbf{R}_h^p z_{\tau h}. \quad (26)$$

Taking the above into consideration, we then obtain the temporal and spatial error estimators

$$\eta_\tau := \frac{1}{2} \rho_\tau(u_{\tau h}) (\mathbf{E}_\tau^{(r+1)} z_{\tau h} - z_{\tau h}) + \frac{1}{2} \rho_\tau^*(u_{\tau h}, z_{\tau h}) (\mathbf{E}_\tau^{(r+1)} u_{\tau h} - u_{\tau h}), \quad (27a)$$

$$\begin{aligned} \eta_h := & \frac{1}{2} \rho_\tau(u_{\tau h}) (z_{\tau h} - \mathbf{R}_h^p z_{\tau h}) + \frac{1}{2} \rho_\tau^*(u_{\tau h}, \mathbf{R}_h^p z_{\tau h}) (\mathbf{I}_{2h}^{(2p)} u_{\tau h} - u_{\tau h}) \\ & + \frac{1}{2} S(u_{\tau h}) (z_{\tau h} + \mathbf{R}_h^p z_{\tau h}) + \frac{1}{2} S'(u_{\tau h}) (\mathbf{I}_{2h}^{(2p)} u_{\tau h} - u_{\tau h}, \mathbf{R}_h^p z_{\tau h}). \end{aligned} \quad (27b)$$

Finally, the error indicators have to be represented in a localized form in order to mark elements within the adaptive mesh refinement algorithm. Here, we follow the approach of [10, 7], where we recast the estimators in (27) as

$$\eta_\tau = \sum_{n=1}^N \sum_{K \in \mathcal{T}_h^n} \eta_\tau^{K,n}, \quad \eta_h = \sum_{n=1}^N \sum_{K \in \mathcal{T}_h^n} \eta_h^{K,n}. \quad (28)$$

We refer to [15, Sec. 4.3.2] for a detailed derivation of (28) in the context of CDR equations.

4 Anisotropic Method

Convection-dominated problems often exhibit anisotropic solution features (e. g. thin layers with steep gradients). Anisotropic mesh refinement is advantageous in these cases, as interpolation error estimates indicate that approximation errors scale with the mesh width in each coordinate direction multiplied by the corresponding directional derivative norm (cf. [3]). Thus, being able to identify dominant error directions a posteriori, offers the potential to increase computational efficiency compared to isotropic refinement. In this section, we split the isotropic error estimator η_h (cf. (27b)) into directional contributions such that

$$\eta_h := \eta_{h,1} + \eta_{h,2} + \eta_{h,\mathbb{E}},$$

where $\eta_{h,\mathbb{E}}$ is an anisotropic remainder term. Further, we describe the anisotropic mesh adaptation scheme based on the directional error estimators.

4.1 Anisotropic Finite Elements

In order to split the error in directional contributions, we first introduce finite elements with anisotropic polynomial degree. Let $(p_1, \dots, p_d) \in \mathbb{N}^d$ be a multi-index. On the reference element \hat{K} the anisotropic polynomial space is defined as

$$\hat{Q}_{p_1, \dots, p_d}(\hat{K}) := \bigotimes_{i=1}^d \mathcal{P}_{p_i}([0, 1]),$$

where $\mathcal{P}_{p_i}([0, 1])$ denotes the space of univariate polynomials of degree at most p_i . The DoFs are associated with Gauss–Lobatto nodes. The total number of DoFs per element is $N_K^{p_1, \dots, p_d} = \prod_{i=1}^d (p_i + 1)$

1). We note that this is a straightforward generalization of the isotropic case, where for $p_1 = \dots = p_d := p$, we put \hat{Q}_p . For $i \in \{1, \dots, d\}$ and given integers p and q , we define

$$\hat{Q}_i^{p,q} := \hat{Q}^{p_1, \dots, p_d}, \quad p_j = \begin{cases} p, & j \neq i \\ q, & j = i \end{cases}.$$

Further we denote $N_i^{p,q}$ denotes the set of DoFs on the reference element \hat{K} .

4.2 Anisotropic Interpolation and Restriction Operations

In this subsection, we introduce anisotropic interpolation and restriction operators, which are essential for computing the weights in the anisotropic error estimator. Throughout the remainder of this section, we restrict ourselves to the two-dimensional case, i. e. $\Omega \subset \mathbb{R}^2$.

Definition 4.1. For $p \leq q$, the restriction $\hat{R}_i^{q,p} : \hat{Q}_q(\hat{K}) \rightarrow \hat{Q}_i^{p,q}(\hat{K})$ is defined as the unique function such that, for $\hat{v}^q \in \hat{Q}_q(\hat{K})$,

$$\left(\hat{R}_i^{q,p} \hat{v}^q \right) (\hat{N}_j) = \hat{v}^q(\hat{N}_j) \quad \forall \hat{N}_j \in \hat{N}_i^{p,q}. \quad (29)$$

We call $\hat{R}_i^{q,p}$ the anisotropic restriction operator on the reference element \hat{K} in the i -th direction.

Remark 4.2. The finite elements with anisotropic polynomial degrees are only used in local finite element restrictions and interpolations. The global restriction and interpolation operators are defined such that they immediately map back into finite element spaces with isotropic polynomials. Therefore, we omit the explicit definition of the global finite element spaces with anisotropic polynomial degree.

Definition 4.3. The restriction operator in i -th direction $R_i^p : V_h^{2p} \rightarrow V_h^{2p}$ is defined as

$$(R_i^p v_h)(x) := \left(\hat{R}_i^{2p,p} \hat{v}_h \right) \left((\mathbf{T}_K)^{-1}(x) \right) \quad x \in K, K \in \mathcal{T}_h, \quad (30)$$

for $v_h \in V_h^{2p}$ and $\hat{v}_h = \mathbf{T}_K^{-1} \circ v_h$.

Next, we introduce notation for the a posteriori error representation. Firstly we define a local anisotropic remainder term and show that it is of higher order, similar to the remainder terms in the isotropic error estimator (19).

Definition 4.4. Let $\hat{v}_{2p} \in \hat{Q}_{2p}(\hat{K})$. We define

$$\hat{\mathbb{E}}^{2p} \hat{v}_{2p} := \hat{v}_{2p} + \hat{R}^{2p,p} \hat{v}_{2p} - \hat{R}_1^{2p,p} \hat{v}_{2p} - \hat{R}_2^{2p,p} \hat{v}_{2p}$$

as the local anisotropic remainder on the reference element \hat{K} .

We now prove, that the anisotropic remainder is in fact of higher order. For the sake of simplicity and brevity, we restrict ourselves to the case where $p = 1$ and $q = 2$.

Lemma 4.5. Let $d = 2$, $p = 1$ and $q = 2p = 2$. Additionally, let $\hat{v}_{2p} \in \hat{Q}_{2p}(\hat{K})$. For $\hat{\mathbb{E}}^{2p} \hat{v}_{2p}$ as in Definition 4.4 holds

$$(\hat{\mathbb{E}}^{2p} \hat{v}_{2p})(\hat{x}_1, \hat{x}_2) = \frac{1}{4} \frac{\partial^4 \hat{v}_{2p}}{\partial \hat{x}_1^2 \partial \hat{x}_2^2}(\hat{x}_1, \hat{x}_2) \hat{x}_1 \hat{x}_2 (1 - \hat{x}_1)(1 - \hat{x}_2), \quad (\hat{x}_1, \hat{x}_2) \in \hat{K}. \quad (31)$$

Proof. Follows from technical computations with the nodal values and their corresponding functions on \hat{K} and is omitted for the convenience of the reader. \square

Definition 4.6. Let $v_h \in V_h^{2p}$. We define

$$(\mathbb{E}^{2p} v_h)(x) := \left(\hat{\mathbb{E}}^{2p} \hat{v}_h \right) (\mathbf{T}_K^{-1}(x)) , \quad x \in K, K \in \mathcal{T}_h. \quad (32)$$

as the isotropic remainder in space.

Next we estimate the anisotropic remainder term for arbitrary $K \in \mathcal{T}_h$. Here we restrict ourselves to affine mappings \mathbf{T}_K with a diagonal matrix.

Theorem 4.7. Let $p = 1$ and $K \in \mathcal{T}_h$ with $K = (\tilde{x}_{1,K}, \tilde{x}_{2,K}) + [0, h_{1,K}] \times [0, h_{2,K}]$ for some $\tilde{x}_{1,K}, \tilde{x}_{2,K}$. Furthermore, let $\mathbf{T}_K : \hat{K} \rightarrow K$ be defined as $\mathbf{T}_K(\hat{x}_1, \hat{x}_2) := (x_1, x_2) := (\tilde{x}_{1,K} + \hat{x}_1 h_{1,K}, \tilde{x}_{2,K} + \hat{x}_2 h_{2,K})$. Then for an arbitrary $v_h \in V_h^{2p}$ holds that

$$|\mathbb{E}^{2p} v_h| \leq \frac{1}{16} \sup_{K \in \mathcal{T}_h, (x_1, x_2) \in K} \left| \frac{\partial^4 v_h|_K}{\partial x_1^2 \partial x_2^2}(x_1, x_2) \right| h_{1,K}^2 h_{2,K}^2. \quad (33)$$

Proof. Let $v_h \in V_h^{2p}$ and $K \in \mathcal{T}_h$. Furthermore, let $\hat{v}_{2p} = \mathbf{T}_K^{-1} \circ v_h|_K$. Therefore, we get for all $(\hat{x}_1, \hat{x}_2) \in \hat{K}$ that

$$\begin{aligned} |\hat{\mathbb{E}}^{2p} \hat{v}_{2p}(\hat{x}_1, \hat{x}_2)| &= \frac{1}{4} \left| \frac{\partial^4 \hat{v}_{2p}}{\partial \hat{x}_1^2 \partial \hat{x}_2^2}(\hat{x}_1, \hat{x}_2) \hat{x}_1 \hat{x}_2 (1 - \hat{x}_1)(1 - \hat{x}_2) \right| \\ &= \frac{1}{4} \left| \frac{\partial^4 v_h|_K}{\partial x_1^2 \partial x_2^2}(\mathbf{T}_K(\hat{x}_1, \hat{x}_2)) h_{1,K}^2 h_{2,K}^2 \hat{x}_1 \hat{x}_2 (1 - \hat{x}_1)(1 - \hat{x}_2) \right| \\ &\leq \frac{1}{4} \left| \frac{\partial^4 v_h|_K}{\partial x_1^2 \partial x_2^2}(\mathbf{T}_K(\hat{x}_1, \hat{x}_2)) h_{1,K}^2 h_{2,K}^2 \right| \frac{1}{4}. \end{aligned}$$

We get that

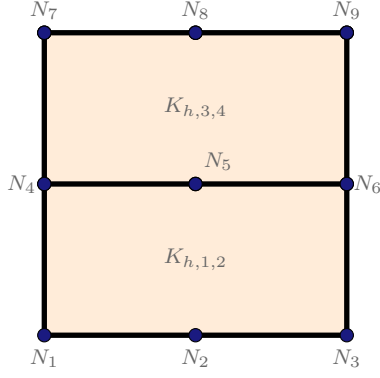
$$|\mathbb{E}^{2p} v_h| \leq \frac{1}{16} \sup_{K \in \mathcal{T}_h, (x_1, x_2) \in K} \left| \frac{\partial^4 v_h|_K}{\partial x_1^2 \partial x_2^2}(x_1, x_2) \right| h_{1,K}^2 h_{2,K}^2. \quad \square$$

Remark 4.8. An extension of Theorem 4.7 to parallelograms as well as a higher polynomial degree $p > 1$ is straight forward.

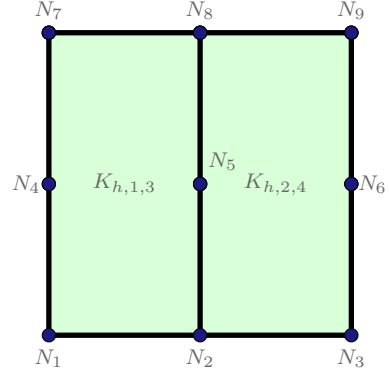
Definition 4.9. For $K_{2h}^P \in \mathcal{T}_{2h}^P$, $K_{2h} \in \mathcal{T}_{2h}$, we define $\mathbb{I}_{2h,i}^{(2p)} : V_h^P(K_{2h}^P) \rightarrow V_h^{2p}(K_{2h})$, the patch-wise higher order interpolation into the spatial direction i , as

$$\mathbb{I}_{2h,i}^{(2p)} := R_i^P \circ \mathbb{I}_{2h}^{(2p)} \quad (34)$$

With abuse of notation, the operator R_i^P (cf. (30)), which was originally defined for elements $K \in \mathcal{T}_h$, is here extended to act on elements $K_{2h} \in \mathcal{T}_{2h}$. Further, the global anisotropic restriction operator is denoted by the same name. The action of directional interpolation operators, where $p = 1$, is visualized in Figure 4 and the DoFs are shown in Figure 3.



(a) $Q_{2,1}$ finite elements on $K_{2h,1*}^P$.



(b) $Q_{1,2}$ finite elements on $K_{2h,2*}^P$.

Figure 3: DoFs of finite elements with anisotropic (a), (b) polynomial degrees on a patch.

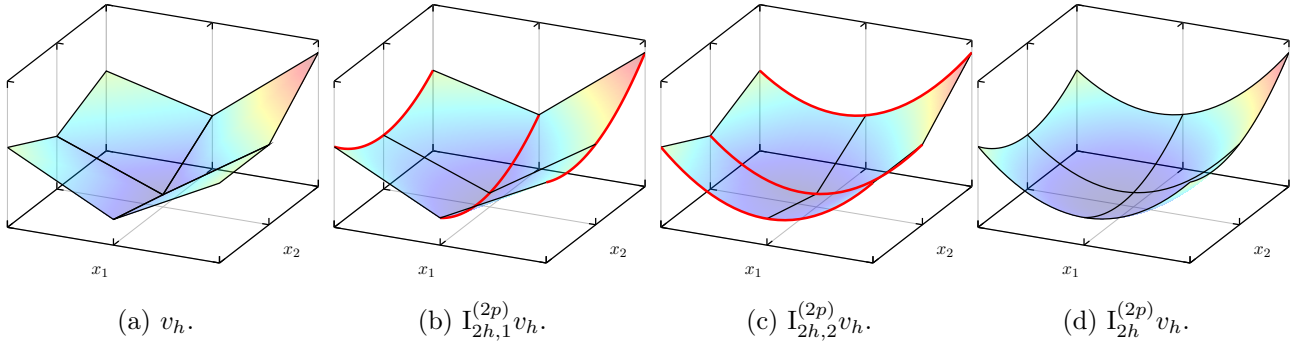


Figure 4: The action of different interpolation operators on a function v_h on the patch K_{2h} and $p = 1$.

4.3 Anisotropic Goal Oriented Error Estimation

In this subsection, we extend the classical error representation from Theorem 3.3 to the anisotropic setting, following the approach introduced by Richter in [47, Theorem 2]. The key idea is the anisotropic splitting of the discretization error into distinct directional contributions, providing the theoretical foundation for anisotropic goal-oriented error estimation. While our framework closely follows the one developed in [47], our contribution is a different approximation of the directional error contributions, which we precisely state in the following theorem.

Theorem 4.10. *Let η_h be defined as in (27). Then, for the splitting into the single directions it holds*

$$\eta_h := \eta_{h,1} + \eta_{h,2} + \eta_{h,\mathbb{E}}, \quad (35)$$

where

$$\begin{aligned} \eta_{h,i} := & \frac{1}{2} \rho_\tau(u_{\tau h})(z_{\tau h} - R_i^p z_{\tau h}) + \frac{1}{2} \rho_\tau^*(u_{\tau h}, z_{\tau h})(I_{2h,i}^{(2p)} u_{\tau h} - u_{\tau h}) \\ & + \frac{1}{2} S(u_{\tau h})(R_i^p z_{\tau h}) + \frac{1}{2} S'(u_{\tau h})(I_{2h,i}^{(2p)} u_{\tau h} - u_{\tau h}, R_h^p z_{\tau h}), \end{aligned} \quad (36)$$

for $i \in \{1, 2\}$ and

$$\begin{aligned} \eta_{h,\mathbb{E}} := & \frac{1}{2} \rho_\tau(u_{\tau h})(\mathbb{E}^{2p} z_{\tau h}) + \frac{1}{2} \rho_\tau^*(u_{\tau h}, R_h^p z_{\tau h})(\mathbb{E}^{2p} I_{2h}^{(2p)} u_{\tau h}) \\ & + \frac{1}{2} S(u_{\tau h})(\mathbb{E}^{2p} z_{\tau h}) + \frac{1}{2} S'(u_{\tau h})(\mathbb{E}^{2p} I_{2h}^{(2p)} u_{\tau h}, R_h^p z_{\tau h}). \end{aligned} \quad (37)$$

Proof. For $v_h \in \mathcal{V}_h^{2p}$, we obtain from the definition of the restrictions (25) and (30), that

$$(I + R_h^p - R_1^p - R_2^p)v_h - \mathbb{E}^{(2p)}v_h = 0, \quad (38)$$

where I is the identity mapping. Adding $(I - R_h^p)v_h$ on both sides of (38), we get

$$v_h - R_h^p v_h = (I - R_1^p)v_h + (I - R_2^p)v_h - \mathbb{E}^{(2p)}v_h. \quad (39)$$

Since by definition $\mathbb{I}_{2h}^{(2p)} R_h^p = I$, it directly follows that for $v_h \in \mathcal{V}_h^{2p}$ we have

$$\mathbb{I}_{2h}^{(2p)} v_h - \underbrace{R_h^p \mathbb{I}_{2h}^{(2p)} v_h}_{=v_h} = (I - R_1^p) \mathbb{I}_{2h}^{(2p)} v_h + (I - R_2^p) \mathbb{I}_{2h}^{(2p)} v_h - \mathbb{E}^{(2p)} \mathbb{I}_{2h}^{(2p)} v_h. \quad (40)$$

Furthermore, from (38) we deduce that

$$(I + R_h^p)v_h = (R_1^p + R_2^p)v_h + \mathbb{E}^{(2p)}v_h. \quad (41)$$

The discrete isotropic error estimator η_h , given in (27), then reads as

$$\begin{aligned} \eta_h = & \frac{1}{2} \rho_\tau(u_{\tau h})(z_{\tau h} - R_h^p z_{\tau h}) + \frac{1}{2} \rho_\tau^*(u_{\tau h}, R_h^p z_{\tau h})(\mathbb{I}_{2h}^{(2p)} u_{\tau h} - u_{\tau h}) \\ & + \frac{1}{2} S(u_{\tau h})(z_{\tau h} + R_h^p z_{\tau h}) + \frac{1}{2} S'(u_{\tau h})(\mathbb{I}_{2h}^{(2p)} u_{\tau h} - u_{\tau h}, R_h^p z_{\tau h}). \end{aligned}$$

We obtain the result by substituting $z_{\tau h} - R_h^p z_{\tau h}$, $\mathbb{I}_{2h}^{(2p)} u_{\tau h} - u_{\tau h}$ and $z_{\tau h} + R_h^p z_{\tau h}$ by the equations (39) to (41), respectively. \square

Remark 4.11. Here $\eta_{h,1}$ and $\eta_{h,2}$ are the directional error estimators. For localization, we employ the classical approach as in [10, 7], analogous to the isotropic error estimator given in (27). A partition of unity technique as in [50, 26, 54, 27, 13, 12] is possible as well.

Remark 4.12. Since, the term $\mathbb{E}^{2p}v_h$ is of higher order (cf. Theorem 4.7), we omit it in our numerical examples and do not restrict ourselves to parallelograms in the experiments (cf. Remark 4.8).

5 Algorithm for Goal-Oriented Anisotropic Mesh Adaptivity

The element wise contributions of the anisotropic error indicators in space and time are given by

$$\eta_\tau = \sum_{n=1}^N \sum_{K \in \mathcal{T}_h^n} \eta_\tau^{K,n}, \quad (42a)$$

$$\eta_h = \sum_{i=1}^d \sum_{n=1}^N \sum_{K \in \mathcal{T}_h^n} \eta_{h,i}^{K,n}, \quad (42b)$$

where we neglect the spatial higher order remainder term of η_h in Theorem 4.10 according to Rem. 4.12 and η_τ is defined in (27a), respectively. These indicators steer the anisotropic mesh adaptation strategy presented in Algorithm 1. There, we use the spatial directional indicators and the temporal indicators to mark spatial elements in each direction and time intervals. This marking results in anisotropic and isotropic refinements.

Algorithm 1 Anisotropic Mesh Adaptation: mark & refine

Require: $\eta_{h,i}^{K,n}, \eta_\tau^{K,n}$ (cf. (42)) for all $K \in \mathcal{T}_h$, for all $I_n \in \mathcal{T}_\tau$, θ_h, θ_τ

- 1: **Calculate** for all $K \in \mathcal{T}_h$, $i = 1, \dots, d$: $\eta_{h,i}^K = \sum_{I_n \in \mathcal{T}_\tau} \eta_{h,i}^{K,n}$.
 - 2: **Calculate** for all $I_n \in \mathcal{T}_\tau$: $\eta_\tau^n = \sum_{K \in \mathcal{T}_h} \eta_\tau^{K,n}$.
 - 3: **for** $i = 1, \dots, d$ **do**
 - 4: **Mark** $\theta_h |\mathcal{T}_h|$ cells $K \in \mathcal{T}_h$ with the largest refinement criteria $\eta_{h,i}^K$ for *refinement in direction i* .
 - 5: **Mark** $\theta_\tau |\mathcal{T}_\tau|$ subintervals $I_n \in \mathcal{T}_\tau$ with the largest refinement criteria η_τ^n for refinement.
 - 6: **Refine** in space according to marking in line 4
 - 7: **Refine** in time according to marking in line 5
-

Remark 5.1 (Anisotropic Mesh Adaptation).

- As the spatial mesh is fixed for all time intervals, the local error indicators $\eta_{h,i}^{K,n}$, computed for each cell K and direction i , are summed over time intervals to yield the total directional error $\eta_{h,i}^K$ (Algorithm 1, line 1). The temporal error η_τ^n results from summing local contributions across all spatial elements (Algorithm 1, line 2).
- Marking for refinement is performed separately in each spatial direction (Algorithm 1, line 4). A spatial element K is marked for refinement in direction i if its directional indicator $\eta_{h,i}^K$ is among the top $\theta_h |\mathcal{T}_h|$ values. Evaluating directional errors individually naturally yields anisotropic refinement when one direction dominates, and isotropic refinement when errors are balanced.
- Adaptive refinement on quadrilateral or hexahedral meshes leads to interdependent hanging nodes. To resolve these mutual dependencies, we refine the coarser element at the end of the hanging-node chain in the appropriate direction (i.e. anisotropically).

To compute the error indicators required in Algorithm 1, we first solve the primal problem forward in time, followed by the adjoint problem backward in time. Using both primal and adjoint solutions, we calculate the local error estimators (42), perform marking and refinement according to Algorithm 1, and repeat the space-time solution procedure iteratively until the desired accuracy is reached. For algorithmic details and implementation aspects, especially regarding space-time finite elements, we refer to [40, 15, 11, 53, 52, 54, 26, 23, 24].

6 Numerical Examples

To validate the efficacy of our anisotropic adaptive mesh refinement approach applied to time-dependent CDR equations, we present three numerical examples.

1. *Interior Layer Problem:* For this benchmark case an exact solution is available, which is characterized by a sharp interior layer.
2. *Stationary Hemker Problem:* The Hemker problem serves as a more challenging test case. It can be interpreted as a model of a convection-dominated heat transfer from a hot column. The

solution to the Hemker problem is characterized by a boundary layer at the cylinder's surface and two interior layers located downstream of the cylinder.

3. *Nonstationary Hemker Problem with quadratic obstacle:* We modify the classical Hemker problem to be nonstationary and replace the circular obstacle by a quadratic one.

In these examples, we employ isotropic and anisotropic refinement strategies. Depending on the refinement type, a different marking strategy is employed. In the case of isotropic refinement, dynamic meshes are used, i.e. the mesh can be different between timesteps. Thereby, each time slab has its own mesh. Conversely, the anisotropic mesh refinement strategy only allows fixed meshes in time at the current stage of development.

To measure the accuracy of the error estimator we will study the *effectivity index*

$$I_{\text{eff}}^a = \left| \frac{\eta_{h,x} + \eta_{h,y} + \eta_\tau}{J(u) - J(u_{\tau h})} \right|, \quad I_{\text{eff}} = \left| \frac{\eta_h + \eta_\tau}{J(u) - J(u_{\tau h})} \right|, \quad (43)$$

for the anisotropic and isotropic case, respectively. For the anisotropic case, we further denote $\eta_h^a = \eta_{h,x} + \eta_{h,y}$ and $\eta_{\tau h}^a = \eta_\tau + \eta_h^a$, where $\eta_{h,x} := \eta_{h,1}$ and $\eta_{h,y} := \eta_{h,2}$. For the isotropic case we denote $\eta_{\tau h} = \eta_\tau + \eta_h$. Moreover, as an indicator for the anisotropy we consider the maximum *aspect ratio*, given by

$$\text{ar}_{\max} := \max_{K \in \mathcal{T}_h} \max_{\mathbf{x} \in Q_K} \frac{\lambda_{\max}}{\lambda_{\min}}, \quad (44)$$

where Q_K is the set of quadrature points on N_{time} and $\lambda_{\min}, \lambda_{\max}$ are the minimal and maximal eigenvalues of $\nabla \mathbf{T}_K(\mathbf{x})$, respectively. The SUPG stabilization parameter $\delta_K(\cdot)$ is defined as

$$\delta_K = \delta_0 h_K,$$

where $h_K = \sqrt[d]{|K|}$ is the cell diameter of the mesh cell. Throughout this work we choose $\delta_0 = 0.1$. The total number of DoFs is denoted by N_{tot} , whereas the spatial DoFs and temporal DoFs are denoted by N_{space} and N_{time} , respectively. The implementation is based on the `deal.II` finite element library [1]. The tests are run on a single node with 2 Intel Xeon Platinum 8360Y CPUs and 1024 GB RAM of the HPC cluster HSUper at HSU.

6.1 Interior Layer Problem

This well-known benchmark with a sharp interior layer of thickness $\mathcal{O}(\sqrt{\varepsilon} |\log \varepsilon|)$ has an exact solution

$$u(\mathbf{x}, t) = \frac{e^{3(t-1)}}{2} \left(1 - \tanh \frac{2x - y - \frac{1}{2}}{\sqrt{5\varepsilon}} \right). \quad (45)$$

The problem is defined on $\mathcal{Q} := \Omega \times I = (0, 1)^2 \times (0, 1]$ with inhomogeneous boundary conditions given by (45) on the whole spatial boundary $\Gamma_D = \partial\Omega$. The convection is set to $\mathbf{b} = \frac{1}{\sqrt{5}}(1, 2)^\top$, the diffusion to $\varepsilon = 1 \times 10^{-6}$ and the reaction coefficient is given by $\alpha = 1$. As sketched in Figure 5, we use structured and unstructured meshes with isotropic and anisotropic refinement. In all configurations, we refine and coarsen a fixed fraction of cells in both space and time. In space, the refinement fraction is set to $\theta_{\text{space}}^{\text{ref}} = \frac{1}{5}$, and the coarsening fraction is $\theta_{\text{space}}^{\text{co}} = \frac{1}{100}$. Similarly, in time, the refinement

fraction is $\theta_{\text{time}}^{\text{ref}} = \frac{2}{3}$, while no coarsening is applied, i.e., $\theta_{\text{time}}^{\text{co}} = 0$. Finally, the goal functional is chosen to control the global $L^2(L^2)$ -error in space and time, given by

$$J(u) = \frac{1}{\|e\|_{\mathcal{Q}}} \int_I (u, e) dt, \quad \text{with } \|\cdot\|_{\mathcal{Q}} = \left(\int_I (\cdot, \cdot) dt \right)^{\frac{1}{2}}, \quad e := u - u_{\tau h}. \quad (46)$$

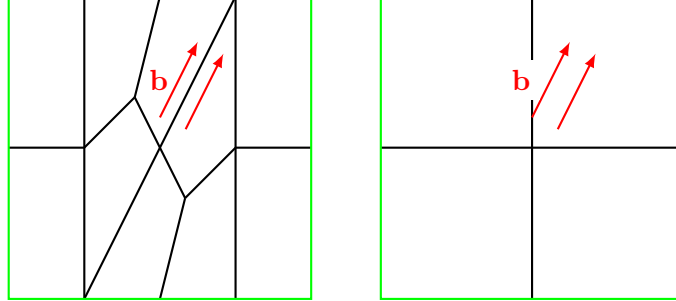


Figure 5: Geometry and coarse, unstructured (left) and structured (right) spatial mesh of the domain Ω for Example 6.1.

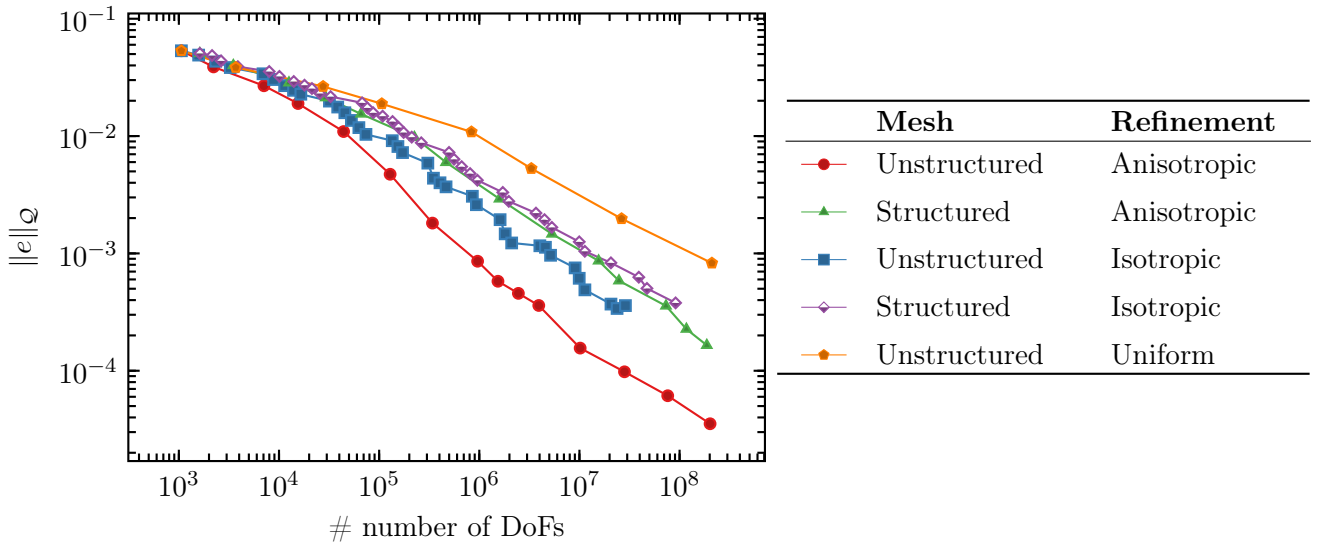


Figure 6: A comparison of the different refinement strategies and meshes in terms of their efficiency measured by the error over the number of space-time DoFs.

Figure 6 compares the convergence behavior of the error norm $\|e\|_{\mathcal{Q}}$ versus the number of DoFs for various mesh refinement strategies. The anisotropic and isotropic refinements are clearly superior to the uniform refinement on an unstructured mesh. In addition, the anisotropic refinement on unstructured and structured meshes exhibits a faster error reduction per DoF than their isotropic counterparts. Overall, we confirm that anisotropic adaptive refinement achieves superior accuracy with fewer DoFs, which is crucial for efficiently resolving convection-dominated phenomena.

In Figure 7, we present the solution profiles and spatial meshes at final time $T = 1$ regarding the different refinement strategies on an unstructured mesh. With regard to over- and undershoots, which is an important measure for spurious oscillations for convection-dominated problems, we obtain the following results.

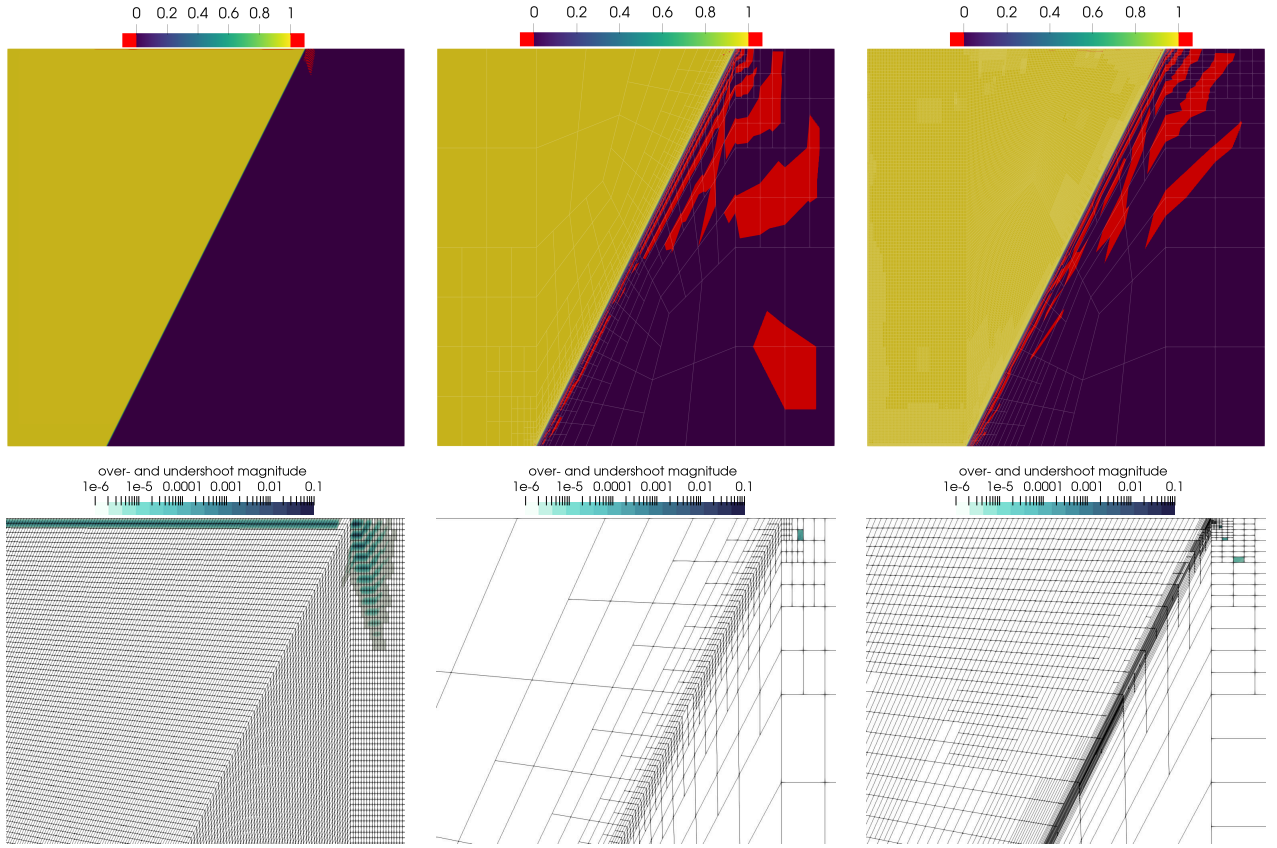


Figure 7: All solutions obtained using three different approaches: uniform refinement, isotropic adaptive refinement, and anisotropic adaptive refinement. Over- and undershoots are highlighted in red, independent of their magnitude. The second row illustrates the magnitude of the over- and undershoots in the subdomain $[0.63, 0.88] \times [0.77, 1.0]$. Only regions where the over- and undershoot is larger than 1×10^{-6} are plotted.

Over- and Undershoots We measure the over- and undershoots in the last DWR loop at final time $T = 1$, where the solution lies within the range $[0, 1]$. Uniform refinement yields an undershoot of 0.0153 and an overshoot of 0.0044 at a maximum of 656 897 spatial DoFs. Isotropic adaptive refinement reduces them to 0.0063 and 0.0074, respectively, at a maximum of 43 143 spatial DoFs. The most favorable results are obtained with anisotropic adaptive refinement, which produces an undershoot of 7.329×10^{-4} and an overshoot of 2.9397×10^{-4} at a maximum of 43 143 spatial DoFs. Comparing the spatial meshes in Figure 7, we observe a significantly higher concentration of elements at the interior layer for the anisotropic adaptive refinement compared to the other strategies.

In Tables 1–5 we compare the errors and effectivity indices for the different refinement strategies. In Table 1 (unstructured anisotropic), the error norm $\|e\|_{(0,T) \times \Omega}$ decreases to 3.53×10^{-5} within 15 DWR loops. Cells become increasingly stretched in the direction of the interior layer due to the anisotropic mesh refinement. Consequently, the maximal aspect ratio ar_{\max} increases from 4 to 841. The effectivity index I_{eff} remains bounded and relatively close to 1.

Table 2 (structured anisotropic) also shows efficient error reduction. Since the structured grid is not aligned with the interior layer, finer meshes are required to achieve errors comparable to the

unstructured anisotropic case. The maximal aspect ratio remains lower, which reflects the limitations imposed by the missing alignment of the mesh with the interior layer. Overall, the anisotropic error estimators are well balanced and reliably track the true error while using fewer DoFs compared to the other strategies (cf. Tables 3–5).

In contrast, Tables 3, 5 and 4 (isotropic refinement on unstructured and structured meshes and uniform refinement) show a noticeably slower decrease in the error norm. The tables confirm the observations in Figure 6. In all cases, the effectivity indices are satisfactory.

Table 1: *Anisotropic* adaptive refinement on an *unstructured* mesh including effectivity indices, error indicators and maximum aspect ratios for goal quantity (46), $\varepsilon = 10^{-6}$, $\delta_0 = 0.1$ for Example 6.1.

ℓ	N_{tot}	N_{space}	N_{time}	$\ e\ _{\mathcal{Q}}$		$\eta_{h,x}$	$\eta_{h,y}$	η_h	η_τ	$\eta_{\tau h}$	I_{eff}^a	ar_{max}
1	1060	53	20	5.333e-02	-	6.143e-03	9.954e-03	1.609e-02	2.584e-03	1.868e-02	0.35	4
2	2220	111	20	3.886e-02	0.46	4.275e-03	6.451e-03	1.072e-02	3.798e-03	1.452e-02	0.37	7
3	7072	221	32	2.683e-02	0.53	4.144e-03	4.728e-03	8.871e-03	1.533e-03	1.040e-02	0.39	14
4	15 488	484	32	1.894e-02	0.50	2.901e-03	2.829e-03	5.730e-03	2.189e-03	7.919e-03	0.42	15
5	44 166	866	51	1.092e-02	0.79	1.848e-03	1.745e-03	3.593e-03	1.078e-03	4.672e-03	0.43	29
6	128 709	1589	81	4.726e-03	1.21	1.147e-03	1.169e-03	2.317e-03	9.179e-04	3.234e-03	0.68	30
7	340 689	2641	129	1.812e-03	1.38	2.341e-04	2.417e-04	4.758e-04	1.116e-03	1.591e-03	0.88	53
8	962 020	4670	206	8.577e-04	1.08	-1.003e-04	-1.241e-04	-2.244e-04	9.001e-04	6.757e-04	0.79	105
9	1 536 430	4670	329	5.790e-04	0.57	6.604e-06	-2.690e-05	-2.030e-05	5.010e-04	4.807e-04	0.83	105
10	2 456 420	4670	526	4.564e-04	0.34	-1.882e-05	-6.018e-05	-7.900e-05	3.099e-04	2.309e-04	0.51	105
11	3 927 470	4670	841	3.600e-04	0.34	5.735e-05	5.731e-06	6.308e-05	1.321e-04	1.952e-04	0.54	105
12	10 168 200	7560	1345	1.559e-04	1.21	-1.777e-05	-3.096e-05	-4.873e-05	1.174e-04	6.872e-05	0.44	211
13	28 176 136	13 093	2152	9.794e-05	0.67	-1.176e-04	-1.232e-04	-2.408e-04	9.128e-05	-1.495e-04	1.53	380
14	76 159 160	22 120	3443	6.125e-05	0.68	-6.369e-05	-7.054e-05	-1.342e-04	4.856e-05	-8.567e-05	1.40	421
15	201 631 356	36 607	5508	3.534e-05	0.79	-3.968e-05	-4.136e-05	-8.105e-05	3.086e-05	-5.018e-05	1.42	841

Table 2: *Anisotropic* adaptive refinement on a *structured* mesh including effectivity indices, error indicators and maximum aspect ratios for goal quantity (46), $\varepsilon = 10^{-6}$, $\delta_0 = 0.1$ for Example 6.1.

ℓ	N_{tot}	N_{space}	N_{time}	$\ e\ _{\mathcal{Q}}$		$\eta_{h,x}$	$\eta_{h,y}$	η_h	η_τ	$\eta_{\tau h}$	I_{eff}^a	ar_{max}
1	1620	81	20	5.065e-02	-	9.973e-03	1.651e-03	1.162e-02	2.463e-03	1.408e-02	0.28	1
5	65 856	2058	32	1.544e-02	0.46	5.445e-03	1.674e-03	7.120e-03	2.607e-03	9.727e-03	0.63	4
6	224 859	4409	51	9.755e-03	0.66	4.846e-03	1.723e-03	6.569e-03	1.138e-03	7.708e-03	0.79	8
7	465 630	9130	51	5.972e-03	0.71	3.254e-03	1.408e-03	4.662e-03	1.885e-03	6.548e-03	1.10	8
8	1 590 111	19 631	81	2.917e-03	1.03	1.539e-03	8.821e-04	2.421e-03	1.423e-03	3.845e-03	1.32	8
9	5 316 993	41 217	129	1.465e-03	0.99	2.420e-04	1.627e-04	4.047e-04	1.389e-03	1.794e-03	1.23	16
10	15 538 580	75 430	206	8.646e-04	0.76	9.463e-05	5.731e-05	1.519e-04	8.977e-04	1.049e-03	1.21	16
11	24 816 470	75 430	329	5.850e-04	0.56	1.774e-04	1.186e-04	2.960e-04	4.899e-04	7.860e-04	1.34	16
12	73 151 872	139 072	526	3.571e-04	0.71	-1.352e-05	-2.024e-05	-3.376e-05	3.872e-04	3.534e-04	0.99	16
13	116 959 552	139 072	841	2.265e-04	0.66	4.424e-06	-7.214e-06	-2.790e-06	2.097e-04	2.069e-04	0.91	16
14	187 051 840	139 072	1345	1.649e-04	0.46	4.296e-05	2.593e-05	6.889e-05	1.076e-04	1.765e-04	1.07	16

Table 3: *Isotropic* adaptive refinement on an *unstructured* mesh including effectivity indices and error indicators for goal quantity (46), $\varepsilon = 10^{-6}$, $\delta_0 = 0.1$ for Example 6.1.

ℓ	N_{tot}	N_{space}	N_{time}	$\ e\ _{(0,T) \times \Omega}$		η_h	η_τ	$\eta_{\tau h}$	I_{eff}
1	1060	53	20	5.3333e-02	-	1.9008e-02	2.5843e-03	2.1592e-02	0.405
20	348 413	3819	129	4.3748e-03	0.43	2.1016e-03	3.8237e-04	2.4840e-03	0.568
21	405 133	4427	129	3.9994e-03	0.13	1.6850e-03	4.2606e-04	2.1111e-03	0.528
22	465 675	5195	129	3.6932e-03	0.11	1.2406e-03	4.5936e-04	1.7000e-03	0.460
26	1 813 955	9791	329	1.4684e-03	0.40	8.1342e-04	1.7237e-04	9.8579e-04	0.671
27	2 105 527	11 315	329	1.2275e-03	0.26	7.6551e-04	2.2961e-04	9.9513e-04	0.811
28	4 025 176	13 299	526	1.1618e-03	0.08	5.8804e-04	1.0736e-04	6.9539e-04	0.599
33	11 337 819	29 493	841	4.8914e-04	0.33	2.2268e-04	9.1019e-05	3.1370e-04	0.641
34	20 654 385	33 035	1345	3.6996e-04	0.40	2.4201e-04	4.3546e-05	2.8555e-04	0.772
35	23 761 175	43 143	1345	3.3944e-04	0.12	2.1303e-04	4.8844e-05	2.6188e-04	0.772

Table 4: *Global space-time* mesh refinement on an *unstructured* mesh including effectivity indices and error indicators for goal quantity (46), $\varepsilon = 10^{-6}$, $\delta_0 = 0.1$ for Example 6.1.

ℓ	N_{tot}	N_{space}	N_{time}	$\ e\ _{(0,T) \times \Omega}$		η_h	η_τ	$\eta_{\tau h}$	I_{eff}
1	1060	53	20	5.3333e-02	-	1.9008e-02	2.5843e-03	2.1592e-02	0.405
2	3700	185	20	3.8446e-02	0.47	1.3415e-02	3.9320e-03	1.7347e-02	0.451
3	27 560	689	40	2.6465e-02	0.54	9.4822e-03	1.6755e-03	1.1158e-02	0.422
4	106 280	2657	40	1.8854e-02	0.49	6.1267e-03	2.3485e-03	8.4752e-03	0.450
5	834 640	10 433	80	1.0852e-02	0.80	3.9685e-03	1.0812e-03	5.0497e-03	0.465
6	3 307 600	41 345	80	5.2902e-03	1.04	2.1262e-03	2.1816e-03	4.3078e-03	0.814
7	26 337 440	164 609	160	1.9767e-03	1.42	6.1838e-04	1.4855e-03	2.1039e-03	1.064
8	210 207 040	656 897	320	8.2674e-04	1.26	8.6590e-05	8.9817e-04	9.8476e-04	1.191

Table 5: *Isotropic* adaptive refinement on an *structured* mesh including effectivity indices and error indicators for goal quantity (46), $\varepsilon = 10^{-6}$, $\delta_0 = 0.1$ for Example 6.1.

ℓ	N_{tot}	N_{space}	N_{time}	$\ e\ _{(0,T) \times \Omega}$		η_h	η_τ	$\eta_{\tau h}$	I_{eff}
1	1620	81	20	5.0651e-02	-	1.1831e-02	2.4635e-03	1.4294e-02	0.282
24	809 029	13 067	81	4.7925e-03	0.20	2.9181e-03	8.1319e-04	3.7313e-03	0.779
25	957 281	15 391	81	4.2042e-03	0.19	2.3924e-03	9.4366e-04	3.3361e-03	0.794
26	1 716 843	16 939	129	3.3112e-03	0.34	2.0590e-03	5.7717e-04	2.6362e-03	0.796
27	1 971 045	21 699	129	2.7787e-03	0.25	1.7044e-03	6.9268e-04	2.3971e-03	0.863
28	3 681 232	27 849	206	2.2060e-03	0.33	1.6903e-03	3.2951e-04	2.0198e-03	0.916
29	4 481 050	31 829	206	1.9394e-03	0.19	1.4083e-03	3.7049e-04	1.7788e-03	0.917
30	5 302 584	34 857	206	1.6684e-03	0.22	1.0610e-03	4.3793e-04	1.4989e-03	0.898
34	39 173 901	76 007	841	6.2703e-04	0.41	3.8103e-04	6.7582e-05	4.4862e-04	0.715
35	47 231 743	90 559	841	5.0324e-04	0.32	2.7943e-04	8.5870e-05	3.6530e-04	0.726
36	91 245 257	104 407	1345	3.7876e-04	0.41	2.1721e-04	4.0112e-05	2.5732e-04	0.679

6.2 Stationary Hemker Problem

We study the classical Hemker problem introduced in [34]. It consists of the convection diffusion system (1) with $\alpha = 0$, $f = 0$ and without the time derivative. Here, we set $\varepsilon = 1 \times 10^{-4}$. The concentration is entirely advected through the domain without any inherent degradation of the species concentration. Consequently, any decrease in concentration arises solely from numerical artifacts, aside from a negligible reduction caused by the diffusion term. The computational domain is defined as $\Omega = ((-3, 8) \times (-3, 3)) \setminus \{(x, y) | x^2 + y^2 \leq 1\}$, illustrated with the coarse mesh in Figure 8. The boundaries colored green in Figure 8 correspond to Dirichlet boundary conditions. Specifically, the boundary at $x = -3$ is subjected to homogeneous Dirichlet conditions $u = 0$. The boundaries colored blue indicate homogeneous Neumann boundary conditions $\partial_{\mathbf{n}} u = 0$. On the circular boundary, inhomogeneous Dirichlet boundary conditions are imposed with $u = 1$. The refinement fraction is set to $\theta_{\text{space}}^{\text{ref}} = \frac{1}{3}$, and the coarsening fraction is $\theta_{\text{space}}^{\text{co}} = 0$. Here, we use the following goal functional given by

$$J(u) = \int_{\Omega} u \, d\mathbf{x}. \quad (47)$$

The presence of sharp boundary and interior layers is further substantiated in Figure 9, where the left

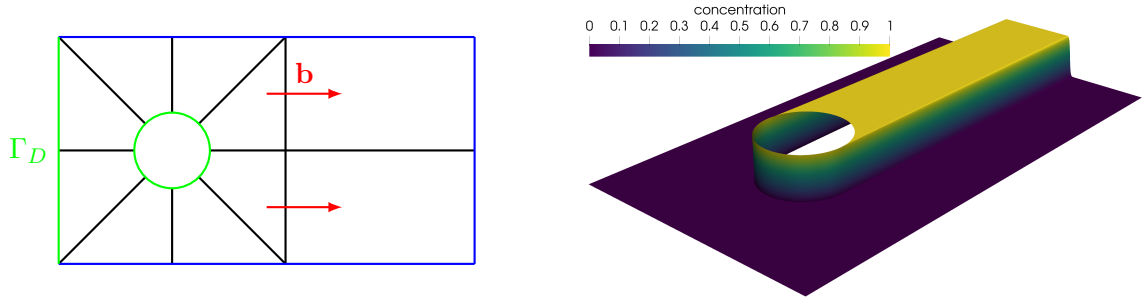


Figure 8: Geometry and coarse mesh of the domain for the Hemker problem (left) and the best adaptive solution obtained in this work (right). In the sketch of the geometry, green coloring corresponds to Dirichlet BCs, while blue indicates homogeneous Neumann BCs. On the circle, inhomogeneous Dirichlet BCs are prescribed. The left boundary is associated with homogeneous Dirichlet BCs.

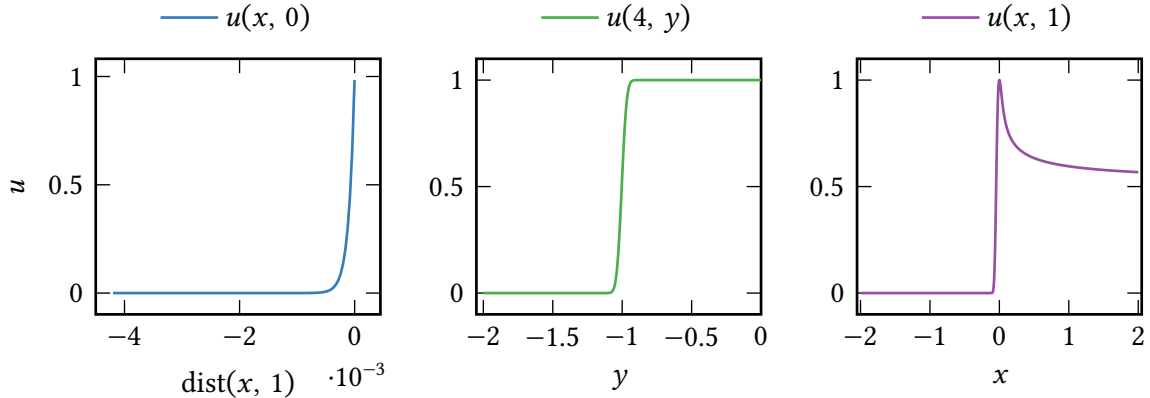


Figure 9: Cut lines of the solution to the Hemker problem. On the left we plot the boundary layer in front of the obstacle. In the middle we plot a cut through one of the interior layers. On the right we plot the solution tangential to the obstacle and within the interior layer.

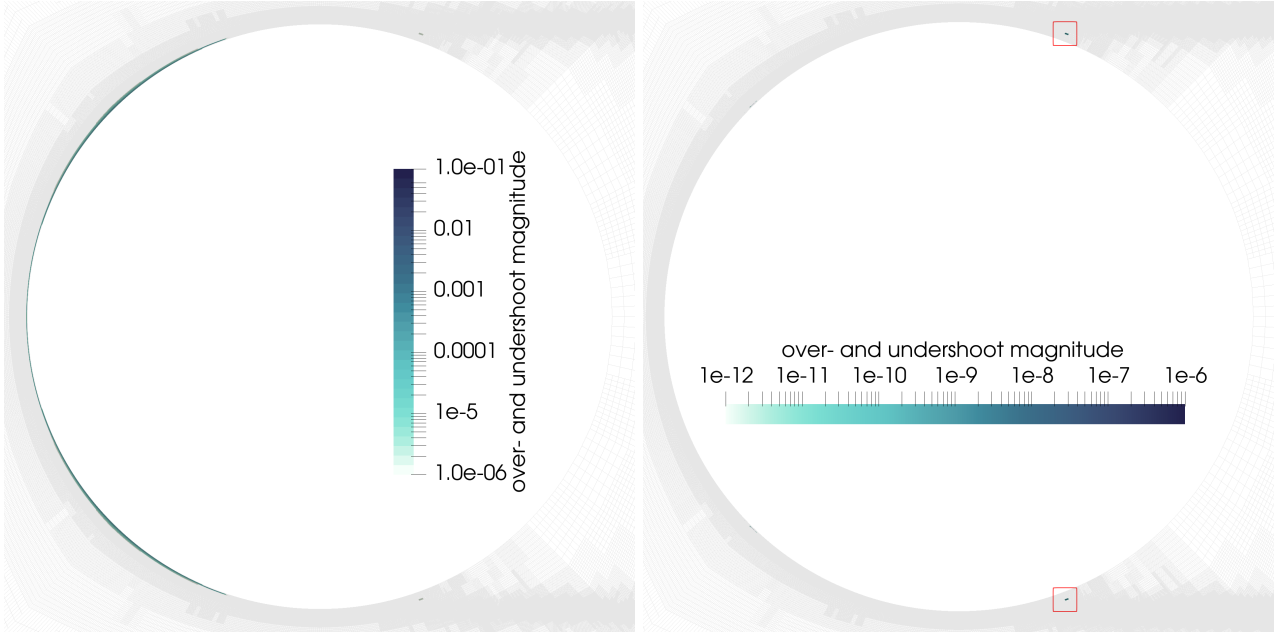


Figure 10: The magnitude of the over- and undershoots in the DWR loop 10 (left) and 11 (right). The maximal magnitude decreases from 7.978×10^{-2} to 2.164×10^{-6} . Only regions where the over- and undershoot is larger than 1×10^{-6} are plotted.

plot shows the boundary layer in front of the obstacle, the middle plot provides a cut through an interior layer, and the right plot illustrates the solution tangential to the obstacle and within the interior layer. All cut lines confirm the correct resolution of the layers within the solution profile with significantly reduced oscillations. Table 6 quantifies the evolution of the spatial error indicators, over successive DWR loops, showing a consistent reduction in error magnitude and an increase in the maximum aspect ratio from approximately 3.8 to 14.3. Figure 10 compares the over- and undershoot magnitudes between DWR loops 10 and 11, demonstrating a dramatic decrease in the maximal undershoot from 7.978×10^{-2} to 2.164×10^{-6} . We emphasize that the undershoot of 2.164×10^{-6} is achieved at only 3061518 DoFs. In the 12th DWR loop maximal over- and undershoot magnitude is further reduced to 3.338×10^{-8} . The width of the interior layer,

$$y_{\text{layer}} = y_1 - y_0, \quad (48)$$

is defined to be the length of the interval $[y_0, y_1]$ in which the solution falls from $u(4, y_0) = 0.9$ to $u(4, y_1) = 0.1$. John et al. [6] provide a reference value of $y_{\text{layer}} = 0.0723$, which we achieve exactly from DWR loop 11 on (cf. Table 6). Overall, these results confirm that the goal-oriented adaptive strategy effectively resolves the critical features of the solution, such as boundary and interior layers, while simultaneously minimizing numerical artifacts.

Table 6: Anisotropic adaptive refinement including directional error indicators, maximum aspect ratios and the layer width over the DWR loops for Example 6.2, $\varepsilon = 10^{-4}$, $\delta_0 = 0.1$.

ℓ	N_{tot}	$\eta_{h,x}$	$\eta_{h,y}$	η_h	ar_{max}	y_{layer}
1	414	-3.47e-01	-2.09e-01	-5.59e-01	3.81	0.7547
2	1412	-1.56e-01	7.83e-02	-7.77e-02	3.97	0.5997
3	3480	-8.70e-02	1.38e-02	-7.31e-02	5.95	0.5747
4	8780	-2.11e-01	-1.51e-01	-3.61e-01	5.97	0.3612
5	22 534	4.58e-02	7.20e-02	1.18e-01	6.81	0.2017
6	53 386	-1.01e-02	-2.65e-03	-1.27e-02	7.52	0.1154
7	121 062	1.85e-03	2.53e-03	4.39e-03	14.25	0.0883
8	272 362	-1.25e-04	-3.26e-04	-4.52e-04	14.25	0.0720
9	621 254	-2.26e-04	-3.24e-04	-5.50e-04	14.25	0.0727
10	1 380 502	-1.77e-04	-2.30e-04	-4.06e-04	14.25	0.0725
11	3 061 518	-1.21e-04	-1.42e-04	-2.63e-04	14.27	0.0723
12	7 054 500	-5.98e-05	-5.95e-05	-1.19e-04	14.27	0.0723

6.3 Nonstationary Hemker Problem with Quadratic Obstacle

In a third example, we study a modified Hemker problem by a quadratic obstacle in a nonstationary setting. Here, in contrast to Sec. 6.2, we set $\varepsilon = 1 \times 10^{-6}$. The computational domain is defined as $\Omega = ((-3, 8) \times (-3, 3)) \setminus \{(x, y) | \max(x, y) \leq 1\}$. On the quadratic obstacle, inhomogeneous Dirichlet boundary conditions are imposed with $u = 1$. The refinement fractions are set to $\theta_{\text{space}}^{\text{ref}} = \frac{1}{6}$, $\theta_{\text{time}}^{\text{ref}} = \frac{1}{10}$, and the coarsening fraction is $\theta_{\text{space}}^{\text{co}} = 0$. The aim is to control the error within a control point $\mathbf{x}_e = (4, 1)$, which is located within the upper interior layer. Thus, we use the goal functional

$$J(u) = u(\mathbf{x}_e). \quad (49)$$

We regularize J by a regularized Dirac delta function $\delta_{r,c}(\mathbf{x}) = \alpha e^{(1-1/(1-r^2/s^2))}$, where $r = \|\mathbf{x} - \mathbf{c}\|$, $s > 0$ is the cutoff radius and α the scaling factor, such that $\delta_{r,c}$ integrates to 1. This test case is solved using the Q_2 elements for the primal and Q_4 elements for the adjoint problem.

The cut-line plots in Figure 11 provide insight into the effectiveness of the anisotropic adaptive mesh refinement. The plots confirm the smoothness around \mathbf{x}_e and display a degradation downstream, which is consistent with the goal-oriented error control at the control point. Figure 12 illustrates the solution and its over- and undershoot magnitudes. We observe the adaptive mesh refinement in the vicinity of \mathbf{x}_e and regions upstream of \mathbf{x}_e . In Figure 13, the distribution of timestep sizes shows that the smallest timesteps occur for $t \in [6, 7]$, coinciding with the passage of the solution front through the control point \mathbf{x}_e . Moreover, Table 7 quantifies the evolution of the spatial and temporal error estimators over the DWR loops. The convergence of the error estimators can be clearly observed. The maximum aspect ratio of the spatial mesh increases from 3.5 to 256, underscoring the effectiveness of anisotropic refinement.

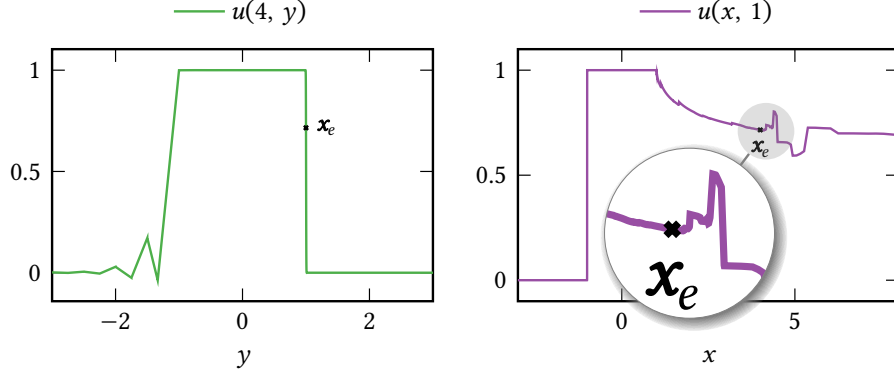


Figure 11: Cut lines of the solution to the nonstationary Hemker problem at final time. On the left, we plot a cut through the interior layers. On the right, we plot a cut tangential to the obstacle and within the upper interior layer. The point of interest is marked in both plots, around which the smoothness of the solution can be observed. In the right plot, we observe that downstream of \mathbf{x}_e , the solution deteriorates. This degradation occurs because the downstream solution has no influence on $u(\mathbf{x}_e)$, and thus on the goal (49).

Table 7: Anisotropic adaptive refinement including directional error indicators for goal quantity (49) and maximum aspect ratios for Example 6.3, $\varepsilon = 10^{-6}$, $\delta_0 = 0.1$.

ℓ	N_{tot}	N_{space}	N_{time}	$\eta_{h,x}$	$\eta_{h,y}$	η_h	η_τ	$\eta_{\tau h}$	ar_{max}
1	576	60	34 560	1.8381e-24	-2.7453e-21	-2.7434e-21	-4.7170e-23	-2.7906e-21	3.5
2	914	66	60 324	-3.0163e-03	-6.4458e-01	-6.4760e-01	-7.6284e-03	-6.5522e-01	3.5
3	1594	72	114 768	-2.1019e-03	-7.6246e-01	-7.6456e-01	-6.7205e-03	-7.7128e-01	4.0
4	2996	79	236 684	-1.7760e-03	-2.6215e-01	-2.6392e-01	-1.8290e-03	-2.6575e-01	8.0
5	4934	86	424 324	-1.6904e-03	-1.1922e-01	-1.2091e-01	-7.0710e-04	-1.2162e-01	16.0
6	8672	94	815 168	-1.4765e-03	-4.4182e-02	-4.5658e-02	-2.1388e-04	-4.5872e-02	16.0
7	14 642	103	1 508 126	-1.0071e-03	-9.2494e-03	-1.0256e-02	-4.1194e-05	-1.0298e-02	16.0
8	25 914	113	2 928 282	-5.2393e-04	-6.2303e-04	-1.1470e-03	-1.0574e-05	-1.1575e-03	32.0
9	44 614	124	5 532 136	-2.9816e-04	-1.2836e-04	-4.2652e-04	-1.3834e-05	-4.4036e-04	64.0
10	73 420	136	9 985 120	-1.7129e-04	-6.9224e-05	-2.4051e-04	-1.5069e-05	-2.5558e-04	128.0
11	112 842	149	16 813 458	-4.8920e-05	-3.9307e-06	-5.2850e-05	-1.5029e-05	-6.7879e-05	256.0

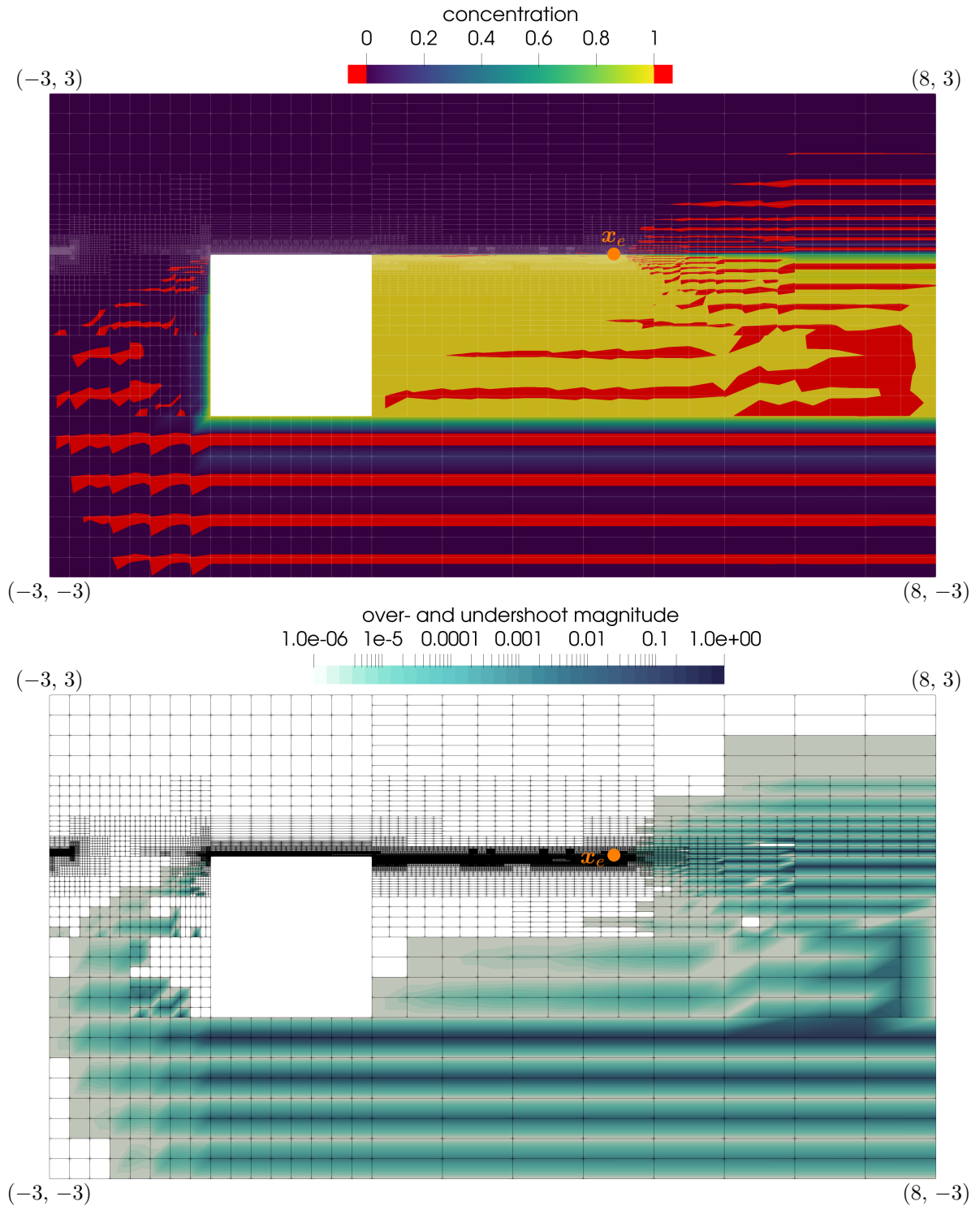


Figure 12: The solution and over- and undershoot magnitude in the final DWR loop for Example 6.3. One can clearly see the adaptive mesh refinement at x_e and upstream of the point due to the goal (49).

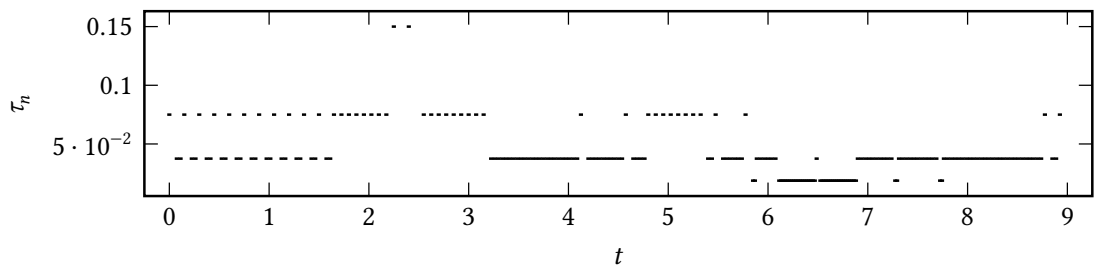


Figure 13: The distribution of timestep sizes over the interval I .

7 Conclusion & Outlook

In this work, we proposed an anisotropic goal-oriented error estimator based on the DWR method for time-dependent CDR equations. The error estimator decouples directional error contributions in space and time while incurring only negligible additional cost compared to the standard DWR approach. Moreover, these error indicators quantify anisotropy of the solution with respect to the goal. SUPG stabilization was applied to suppress spurious oscillations at high Péclet numbers.

The proposed anisotropic adaptive algorithm produces high aspect ratio elements. Consequently, the numerical solutions capture sharp layers without producing spurious oscillations. Numerical experiments confirm that goal-oriented anisotropic refinement in combination with SUPG stabilization outperforms isotropic and global strategies in both accuracy and computational efficiency. The underlying algorithm yields efficient and robust results for multiple challenging benchmarks including both interior and boundary layers. The implementation can address complex geometries by supporting unstructured meshes with curved elements. Therefore, our proposed method effectively controls the error while maintaining feasible problem sizes in the convection-dominated regime.

Currently the implementation only supports tensor-products of a fixed spatial mesh with the temporal mesh. Future work includes the extension to dynamic meshes [53] and quasilinear parabolic problems [57]. Furthermore, an extension to *hp* refinement and discontinuous Galerkin discretizations in space is intended. The methods presented here can be applied to other problems in a straightforward manner.

Acknowledgments

All authors acknowledge the funding of DAAD-project 57729992, "Goal-oriented AnIsotropic Space-Time Mesh Adaption (AIMASIM)" in the funding program "Programm des projektbezogenen Personenaustauschs Griechenland ab 2024". Bernhard Endtmayer and Thomas Wick additionally acknowledge the support by the Cluster of Excellence PhoenixD (EXC 2122, Project ID 390833453). Bernhard Endtmayer was funded by an Humboldt Postdoctoral Fellowship at the beginning of the work. Bernhard Endtmayer thanks the research group of Markus Bause for financing the research visit at the Helmut Schmidt University Hamburg in February 16–28, 2025. Computational resources (HPC cluster HSU-per) have been provided by the project hpc.bw, funded by dtec.bw - Digitalization and Technology Research Center of the Bundeswehr. dtec.bw is funded by the European Union - NextGenerationEU.

Appendix

The explicit definitions of the adjoint bilinear forms in (18) are given by

$$\begin{aligned}
A'(u)(\varphi, z) &= \int_I \{(\varphi, -\partial_t z) + a'(u)(\varphi, z)\} dt + (\varphi(T), z(T)), \\
A'_\tau(u_\tau)(\varphi_\tau, z_\tau) &= \sum_{n=1}^N \int_{I_n} \{(\varphi_\tau, -\partial_t z_\tau) + a'(u_\tau)(\varphi_\tau, z_\tau)\} dt - \sum_{n=1}^{N-1} (\varphi_{\tau,n}^-, [z_\tau]_n) + (\varphi_{\tau,N}^-, z_{\tau,N}^-), \\
A'_S(u_{\tau h})(\varphi_{\tau h}, z_{\tau h}) &= \sum_{n=1}^N \int_{I_n} \{(\varphi_{\tau h}, -\partial_t z_{\tau h}) + a'_h(u_{\tau h})(\varphi_{\tau h}, z_{\tau h})\} dt \\
&\quad + S'(u_{\tau h})(\varphi_{\tau h}, z_{\tau h}) - \sum_{n=1}^{N-1} (\varphi_{\tau h,n}^-, [z_{\tau h}]_n) + (\varphi_{\tau h,N}^-, z_{\tau h,N}^-),
\end{aligned}$$

where the derivative $a'(u)(\varphi, z)$ of the bilinear form $a(u)(z)$ admits the explicit form

$$a'(u)(\varphi, z) = (\varepsilon \nabla \varphi, \nabla z) + (\mathbf{b} \cdot \nabla \varphi, z) + (\alpha \varphi, z).$$

We note that for the representation of $A'(\cdot, \cdot)(\cdot, \cdot)$ integration by parts in time is applied, which is allowed for weak solutions $z \in \mathcal{V}$; cf., e.g., [49, Lemma 8.9].

References

- [1] P. C. Africa, D. Arndt, W. Bangerth, B. Blais, M. Fehling, R. Gassm  ller, T. Heister, L. Heltai, S. Kinnewig, M. Kronbichler, M. Maier, P. Munch, M. Schreter-Fleischhacker, J. P. Thiele, B. Turkcsin, D. Wells, and V. Yushutin. The deal.II library, version 9.6. *Journal of Numerical Mathematics*, 32(4):369–380, 2024.
- [2] N. Ahmed and V. John. Adaptive time step control for higher order variational time discretizations applied to convection-diffusion equations. *Comput. Methods Appl. Mech. Eng.*, 285:83–101, 2015.
- [3] T. Apel. Anisotropic interpolation error estimates for isoparametric quadrilateral finite elements. *Computing*, 60(2):157–174, 1998.
- [4] T. Apel. *Anisotropic Finite Elements: Local Estimates and Applications*. Vieweg+Teubner Verlag, 1999.
- [5] T. Apel and G. Lube. Anisotropic mesh refinement in stabilized galerkin methods. *Numerische Mathematik*, 74(3):261–282, 1996.
- [6] M. Augustin, A. Caiazzo, A. Fiebach, J. Fuhrmann, V. John, A. Linke, and R. Umla. An assessment of discretizations for convection-dominated convection–diffusion equations. *Computer Methods in Applied Mechanics and Engineering*, 200(47):3395–3409, 2011.
- [7] W. Bangerth and R. Rannacher. *Adaptive Finite Element Methods for Differential Equations*. Birkh  user Verlag, Basel, 2003.

- [8] M. Bause, M. P. Bruchhäuser, and U. Köcher. Flexible goal-oriented adaptivity for higher-order space–time discretizations of transport problems with coupled flow. *Comput. Math. Appl.*, 91:17–35, 2021.
- [9] R. Becker and R. Rannacher. A feed-back approach to error control in finite element methods: basic analysis and examples. *East-West J. Numer. Math.*, 4:23–264, 1996.
- [10] R. Becker and R. Rannacher. An optimal control approach to a posteriori error estimation in finite element methods. *Acta Numer.*, 10:1–102, 2001.
- [11] M. Besier and R. Rannacher. Goal-oriented space-time adaptivity in the finite element galerkin method for the computation of nonstationary incompressible flow. *Int. J. Num. Methods Fluids*, 70(9):1139–1166, 2012.
- [12] S. Beuchler, A. Demircan, B. Endtmayer, U. Morgner, and T. Wick. Mathematical modeling and numerical multigoal-oriented a posteriori error control and adaptivity for a stationary, nonlinear, coupled flow temperature model with temperature dependent density. *Computers & Mathematics with Applications*, 175:138–151, 2024.
- [13] S. Beuchler, B. Endtmayer, J. Lankeit, and T. Wick. Multigoal-oriented a posteriori error control for heated material processing using a generalized boussinesq model. *Comptes Rendus. Mécanique*, 351(S1):1–23, 2023.
- [14] A. Brooks and T. Hughes. Streamline upwind/petrov-galerkin formulations for convection dominated flows with particular emphasis on the incompressible navier-stokes equations. *Comput. Methods Appl. Mech. Eng.*, 32(1-3):199–259, 1982.
- [15] M. P. Bruchhäuser. *Goal-oriented space-time adaptivity for a multirate approach to coupled flow and transport*. PhD thesis, Helmut-Schmidt-University/University of the German Federal Armed Forces Hamburg, 2022.
- [16] M. P. Bruchhäuser and M. Bause. A cost-efficient space-time adaptive algorithm for coupled flow and transport. *Comput. Methods Appl. Math.*, 23(4):849–875, 2023.
- [17] M. P. Bruchhäuser and M. Bause. Numerical study of approximation techniques for the temporal weights to the dwr method. In A. e. a. Sequeira, editor, *Numerical Mathematics and Advanced Applications ENUMATH 2023*, Lect. Notes Comput. Sci. Eng. Springer, 2023. accepted.
- [18] M. P. Bruchhäuser, K. Schwegler, and M. Bause. Numerical study of goal-oriented error control for stabilized finite element methods. In *Advanced Finite Element Methods with Applications: Selected Papers from the 30th Chemnitz Finite Element Symposium 2017*, pages 85–106. Springer International Publishing, 2019.
- [19] P. C. Caplan, R. Haimes, D. L. Darmofal, and M. C. Galbraith. Four-dimensional anisotropic mesh adaptation. *Computer-Aided Design*, 129:102915, 2020.

- [20] G. Carey and J. Oden. *Finite elements, computational aspects, Vol. III*. The Texas finite element series. Prentice-Hall, Englewood Cliffs, New Jersey, 1984.
- [21] A. Chakraborty, S. Henneking, and L. Demkowicz. An anisotropic hp -adaptation framework for ultraweak discontinuous petrov–galerkin formulations. *Computers & Mathematics with Applications*, 167:315–327, 2024.
- [22] R. Codina. Comparison of some finite element methods for solving the diffusion-convection-reaction equation. *Computer Methods in Applied Mechanics and Engineering*, 156(1):185–210, 1998.
- [23] W. Dörfler, S. Findeisen, and C. Wieners. Space-time discontinuous galerkin discretizations for linear first-order hyperbolic evolution systems. *Computational Methods in Applied Mathematics*, 16(3):409–428, 2016.
- [24] W. Dörfler, M. Hochbruck, J. Köhler, A. Rieder, R. Schnaubelt, and C. Wieners. A petrov–galerkin space-time approximation for linear hyperbolic systems. In W. Dörfler, M. Hochbruck, J. Köhler, A. Rieder, R. Schnaubelt, and C. Wieners, editors, *Wave Phenomena: Mathematical Analysis and Numerical Approximation*, pages 49–69. Springer International Publishing, 2023.
- [25] B. Endtmayer, U. Langer, T. Richter, A. Schafelner, and T. Wick. A posteriori single- and multi-goal error control and adaptivity for partial differential equations. *Advances in Applied Mechanics (AAMS)*, 59, 2024.
- [26] B. Endtmayer, U. Langer, and A. Schafelner. Goal-oriented adaptive space-time finite element methods for regularized parabolic p -laplace problems. *Computers & Mathematics with Applications*, 167:286–297, 2024.
- [27] B. Endtmayer, U. Langer, and T. Wick. Two-Side a Posteriori Error Estimates for the Dual-Weighted Residual Method. *SIAM J. Sci. Comput.*, 42(1):A371–A394, 2020.
- [28] B. Endtmayer, U. Langer, and T. Wick. Reliability and efficiency of DWR-type a posteriori error estimates with smart sensitivity weight recovering. *Comput. Methods Appl. Math.*, 21(2):351–371, 2021.
- [29] B. Endtmayer and A. Schafelner. Goal oriented adaptive space time finite element methods applied to touching domains. *arXiv preprint arXiv:2401.17237*, 2024.
- [30] L. Formaggia, S. Micheletti, and S. Perotto. Anisotropic mesh adaptation in computational fluid dynamics: application to the advection-diffusion-reaction and the stokes problems. *Appl. Numer. Math.*, 51(4):511–533, 2004.
- [31] L. Formaggia and S. Perotto. New anisotropic a priori error estimates. *Numerische Mathematik*, 89(4):641–667, 2001.

- [32] L. Formaggia, S. Perotto, and P. Zunino. An anisotropic a-posteriori error estimate for a convection-diffusion problem. *Computing and Visualization in Science*, 4(2):99–104, 2001.
- [33] E. H. Georgoulis, E. Hall, and P. Houston. Discontinuous galerkin methods for advection-diffusion-reaction problems on anisotropically refined meshes. *SIAM J. Sci. Comput.*, 2007.
- [34] P. W. Hemker. A singularly perturbed model problem for numerical computation. *Journal of Computational and Applied Mathematics*, 76(1):277–285, 1996.
- [35] T. Hughes and A. Brooks. A multidimensional upwind scheme with no crosswind diffusion. In *Finite Element Methods for Convection Dominated Flows, AMD, vol. 34*, pages 19–35. Amer. Soc. Mech. Engrs. (ASME), 1979.
- [36] V. John, P. Knobloch, and J. Novo. Finite elements for scalar convection-dominated equations and incompressible flow problems: a never-ending story? *Comput. Vis. Sci.*, 19:47–63, 2018.
- [37] V. John and J. Novo. Error analysis of the supg finite element discretization of evolutionary convection-diffusion-reaction equations. *SIAM J. Numer. Anal.*, 49(3):1149–1176, 2011.
- [38] V. John and E. Schmeier. Finite element methods for time-dependent convection-diffusion-reaction equations with small diffusion. *Comput. Methods Appl. Mech. Eng.*, 198(3-4):475–494, 2008.
- [39] P. Knobloch and R. Schneider. On adaptive anisotropic mesh optimization for convection–diffusion problems. *Journal of Computational and Applied Mathematics*, 469:116661, 2025.
- [40] U. Köcher, M. P. Bruchhäuser, and M. Bause. Efficient and scalable data structures and algorithms for goal-oriented adaptivity of space–time FEM codes. *SoftwareX*, 10:100239, 2019.
- [41] R. Kornhuber and R. Roitzsch. On adaptive grid refinement in the presence of internal or boundary layers. *IMPACT of Computing in Science and Engineering*, 2(1):40–72, 1990.
- [42] D. Kuzmin and H. Hajduk. *Property-preserving numerical schemes for conservation laws*. World Scientific, 2024.
- [43] D. Kuzmin, R. Löhner, and S. Turek. *Flux-Corrected Transport: Principles, Algorithms, and Applications*. Scientific Computation. Springer Netherlands, 2012.
- [44] T. Leicht and R. Hartmann. Error estimation and anisotropic mesh refinement for 3d laminar aerodynamic flow simulations. *Journal of Computational Physics*, 229(19):7344–7360, 2010.
- [45] M. Picasso. An anisotropic error indicator based on zienkiewicz–zhu error estimator: Application to elliptic and parabolic problems. *SIAM Journal on Scientific Computing*, 24(4):1328–1355, 2003.
- [46] R. Rannacher and J. Vihharev. Adaptive finite element analysis of nonlinear problems: balancing of discretization and iteration errors. *J. Numer. Math.*, 21(1):23–61, 2013.

- [47] T. Richter. A posteriori error estimation and anisotropy detection with the dual-weighted residual method. *International Journal for Numerical Methods in Fluids*, 62(1):90–118, 2010.
- [48] T. Richter. Anisotropic finite elements for fluid-structure interactions. In A. Cangiani, R. L. Davidchack, E. Georgoulis, A. N. Gorban, J. Levesley, and M. V. Tretyakov, editors, *Numerical Mathematics and Advanced Applications 2011*, pages 63–70. Springer Berlin Heidelberg, 2013.
- [49] T. Richter. *Fluid–structure interactions: Models, analysis and finite elements*, volume 118 of *Lect. Notes Comput. Sci. Eng.* Springer, Berlin, 2017.
- [50] T. Richter and T. Wick. Variational localizations of the dual weighted residual estimator. *J. Comput. Appl. Math.*, 279:192–208, 2015.
- [51] H.-G. Roos, M. Stynes, and L. Tobiska. *Robust numerical methods for singularly perturbed differential equations*. Springer, 2008.
- [52] J. Roth, J. P. Thiele, U. Köcher, and T. Wick. Tensor-Product Space-Time Goal-Oriented Error Control and Adaptivity With Partition-of-Unity Dual-Weighted Residuals for Nonstationary Flow Problems. *Comput. Methods Appl. Math.*, 24(1):185–214, 2024.
- [53] M. Schmich and B. Vexler. Adaptivity with dynamic meshes for space-time finite element discretizations of parabolic equations. *SIAM J. Sci. Comput.*, 30(1):369–393, 2008.
- [54] J. P. Thiele and T. Wick. Numerical Modeling and Open-Source Implementation of Variational Partition-of-Unity Localizations of Space-Time Dual-Weighted Residual Estimators for Parabolic Problems. *J. Sci. Comput.*, 99(25), 2024.
- [55] L. Tobiska and R. Verfürth. Robust a posteriori error estimates for stabilized finite element methods. *IMA Journal of Numerical Analysis*, 35(4):1652–1671, 2015.
- [56] I. Touloupoulos. SUPG space-time scheme on anisotropic meshes for general parabolic equations. *Journal of Numerical Mathematics*, 2024, to appear.
- [57] I. Touloupoulos. A unified space-time finite element scheme for a quasilinear parabolic problem. *Applied Numerical Mathematics*, 214:127–142, 2025.
- [58] M. Yano and D. L. Darmofal. An optimization-based framework for anisotropic simplex mesh adaptation. *Journal of Computational Physics*, 231(22):7626–7649, 2012.
- [59] N. Zander, H. Bériot, C. Hoff, P. Kodl, and L. Demkowicz. Anisotropic multi-level *hp*-refinement for quadrilateral and triangular meshes. *Finite Elements in Analysis and Design*, 203:103700, 2022.